

# We are IntechOpen, the world's leading publisher of Open Access books Built by scientists, for scientists

6,900

Open access books available

186,000

International authors and editors

200M

Downloads

Our authors are among the

154

Countries delivered to

TOP 1%

most cited scientists

12.2%

Contributors from top 500 universities



WEB OF SCIENCE™

Selection of our books indexed in the Book Citation Index  
in Web of Science™ Core Collection (BKCI)

Interested in publishing with us?  
Contact [book.department@intechopen.com](mailto:book.department@intechopen.com)

Numbers displayed above are based on latest data collected.  
For more information visit [www.intechopen.com](http://www.intechopen.com)



## Diversity of Nanofibers from Electrospinning: from Graphitic Carbons to Ternary Oxides.

Yu Wang, Idalia Ramos and Jorge J. Santiago-Aviles  
*University of Pennsylvania and University of Puerto Rico at Humacao,  
 Philadelphia, PA, USA and Humacao, PR.  
 USA*

### 1. Introduction

Electrospinning is a simple method of obtaining polymer fibers with nanoscopic diameter. It uses electrical forces to produce polymer fibers with nanometer scale diameters. Electrospinning occurs when the electrical forces at the surface of an organic solution or melt overcome the surface tension and cause an electrically charged jet to be ejected. As the solvent evaporates, an electrically charged fiber remains. This charged fiber can be directed by electrical forces and then collected in sheets or other useful geometrically forms. In this monograph we are exploring the use of electrospinning in the generation of nanoscopic and microscopic fibers of conductors such as graphitic carbons, semiconductors such as SnO<sub>2</sub>, and insulators such as the Perovskite PZT. The discussion will center mostly in the fibers electrical properties and its applications.

*Carbon Nanofibers:* Carbon nanofibers, like other quasi-one-dimensional nanostructures such as nanowires, nanotubes and molecular wires have potential application in a multiplicity of fields, such as high-temperature catalysis, heat-management materials in aircraft, and filters for separation of small particles from gas or liquid. Of more importance to us, there is a possible use as building blocks for bottom-up assembly applications in nanoelectronics and photonics [Mrozowski, 1979; Hu et al, 1999; Duan et al, 2001]. Carbon fibers are usually produced by spinning from organic precursor fibers or by chemical vapor deposition (CVD). While the spinning method can only produce microscale carbon fibers, CVD can synthesize carbon fibers with diameters from several microns down to less than 100 nm [Bahl et al, 1998; Endo et al, 2001]. However, CVD involves a complicated process and high cost. Electrostatic generation, or electrospinning technique, invented in the 1930s [Formhals, 1934], recently gained renewed interest because it can spin a variety of ultrafine polymer fibers in a micro- or even nanoscale at low cost [Doshi & Reneker, 1995]. By simply pyrolyzing electrospun ultrafine polymer fibers, with a subsequent heat treatment, Chun et al. [Reneker & Chun, 1996] and the authors [Wang et al, 2003] have obtained carbon nanofibers. In general, carbons may include classic carbons such as soot, charcoal, graphite, and “new” carbons. Among the new variants we can mention carbon fibers derived from polyacrylonitrile (PAN), and glass-like carbons derived from nongraphitizable precursors, i.e., various types of more or less crystallized polycrystalline graphites [Iganaki & Radovic, 2002]. These building techniques could overcome fundamental limitations of conventional microfabrication based on lithography [Hu et al, 1999; Duan et al, 2001].

Source: Nanofibers, Book edited by: Ashok Kumar,  
 ISBN 978-953-7619-86-2, pp. 438, February 2010, INTECH, Croatia, downloaded from SCIYO.COM

Carbon fibers have wide applications in structural materials such as composites, and potentially in a multiplicity of nonstructural applications such as sensors [Rebouillat et al, 1999]. The recent “rediscovery” of electrostatic deposition has enabled one to spin a variety of ultra-fine polymer fibers in a simple way, which can be heat treated into carbon fibers with diameter in the nanoscale range [Doshi & Reneker, 1995; Reneker & Chung, 1996; Wang et al, 2002]. The application of carbon nanofibers as sensing elements relies on their electronic transport properties being modulated by the sensing element physico-chemical interaction with the analyte. The authors recently evaluated the size of single electrospun polyacrylonitrile (PAN)-derived carbon nanofibers using a scanning probe microscope for measuring their conductivity at room temperature, and found that the conductivity depends on annealing temperature and time [Wang et al, 2003]

It is well known that the electrical conductivity of pyrolytic graphite increases with temperature. Such temperature dependence was at first explained by the simple two-band (STB) model [Klein, 1964]. The STB model also predicts a level off of the conductivity at a very low temperature. However, recent experimental results show that the conductivity of carbon fibers is very sensitive to temperature at very low values (K) [Bright & Singer, 1979; Spain et al, 1983; Koike & Fukase, 1987]. Such anomaly has been attributed to weak electron localization [Koike & Fukase, 1987], electron-electron interaction [Koike & Fukase, 1987], the Kondo effect [Koike & Fukase, 1987], and hopping mechanism [Baker & Bragg, 1983], all of which show very weak effects unless evaluated at very low temperatures. As to the overall temperature dependence of conductivity, two-dimensional (2-D) weak localization, hopping and tunneling [Abeles et al, 1975] mechanisms have been put forward as possible explanations.

Although classical electron transport theory predicts an increase of electrical resistance in the presence of a magnetic field [Putley, 1960], Mrozowski and Chaberski found a decrease of resistance with magnetic field, or negative magnetoresistance, in partially ordered (pregraphitic) carbons [Mrozowski & Chaberski, 1956]. Since then, negative magnetoresistance has been found not only in poorly graphitized bulk carbon [Hishiyama, 1996] and carbon thin film [Faist & Lohneisen, 2002], but also in carbon fibers, irrespective of whether the carbon fibers were derived from PAN [Koike & Fukase, 1987], benzene [Endo et al, 1982], pitch-derived [Bright & Singer, 1979], or CVD [Fuji et al, 2002]. The most commonly accepted model accounting for the negative magnetoresistance was Bright’s model [Bright, 1979]. This model attributes the resistance decrease to the increase of the density of the states and carrier density with magnetic field, arising from the formation of Landau levels. However, the Bright model cannot account for all of the observed phenomena, including the strong temperature dependence of magnetoresistance below liquid-helium temperature, and the absence of magneto-resistance saturation at high-magnetic field. Then, Bayot et al. [Bayot et al, 1984, 1990] explained the effect using a weak-localization mechanism, which results as a consequence of any small disorder in the electronic system. The weak-localization effects in pregraphitic carbon fibers are due to their turbostatic phase structure, in prior 2-D.

It is noteworthy that the anomalous temperature and magnetic field dependence of conductivity have been found in carbon fibers with diameters larger than 10 nm. It is interesting to evaluate the scaling of such effects, that is, whether similar effects exist in carbon fibers with a diameter of nanoscale although such evaluation becomes increasingly difficult as the diameter is reduced. Note that most of the investigated carbon fibers were heat treatment temperature was higher than 1000 °C, with their observed negative

magnetoresistance of a few percents in magnitude. The weak localization in carbon fiber originates from its disordered nature. By lowering the carbonization temperature, we can probe a lower degree of order in the carbon fiber, and may observe a stronger weak localization effect. In this chapter we comment on the temperature dependence of the electrical conductivity of carbon nanofiber pyrolyzed at a lower temperature of 1273 K, its large negative magnetoresistance at low temperature, and attempt to explain such properties within the frame work of STB and 2D weak-localization models.

#### *Oxide fibers*

*Binary oxides fibers:* Semiconducting tin oxide (stannic oxide,  $\text{SnO}_2$ ), with a rutile structure and a wide bandgap ( $E_g = 3.6$  eV), is chemically inert, mechanically hard, thermally heat-resistant and has a wide variety of existing and potential applications in sensors and optoelectronics such as solar cells, displays and electrochromic devices [Chopra et al, 1983; Williams, 1987]. While the optoelectronics applications of the oxide are mostly due to its wide bandgap, which makes it transparent up to ultraviolet light, its sensor applications are derived from its conductivity modulation by species chemisorbed on its surface and their interaction with non-stoichiometric oxygen vacancies in its lattice. Although the two kinds of applications require  $\text{SnO}_2$  with different nature and levels of crystal defects, such as dopants and oxygen vacancies, both have taken advantage of the thin film morphology, and therefore  $\text{SnO}_2$  thin film has been a research focus. So far, the thin film has been synthesized by various methods, such as evaporation [Seal & Shukla, 2002], sputtering [Shuah & Fun, 1986], spray pyrolysis [Sinclair et al, 1965], chemical vapor deposition [Santhi et al, 1980] and the sol-gel process [Davazoglou, 1997], and its synthetic processes have been characterized and correlated to its final stoichiometry, phase constituents and crystal defects. The preference for thin films in sensor applications is due to its higher surface-to volume ratio than that of the bulk shape and its restriction to the grain growth perpendicular to the substrate. The ratio is even higher and the grain growth is further confined for a fibrous shape. Unfortunately,  $\text{SnO}_2$  fiber has been synthesized in only a limited number of ways, such as by laser ablation [Mishra et al, 2002], thermal decomposition [Liu et al, 2003], oxidizing electrodeposition of a template [Xu et al, 2002] and electrospinning [Kolmakov, 2003]. Of these methods, electrospinning is especially interesting in that it is easy, inexpensive, versatile and flexible. The technique was invented as early as the 1930s [Li et al, 2003] and was recently revitalized to synthesize ultra-fine polymer fibers. We were the first to report the synthesis of micro- and nanoscopic inorganic (lead zirconate titanate) fibers using electrospinning [Wang et al, 2004, Wang & Santiago-Aviles, 2002] and we also developed two recipes for the electrospinning of  $\text{SnO}_2$  fibers: one was modified from that of  $\text{SnO}_2$  thin film fabrication through the sol-gel route [Wang & Santiago-Aviles, 2004] and the other, developed independently, thermally decomposes a single metal-organic, dimethyldineodecanoate tin

( $\text{C}_{22}\text{H}_{44}\text{O}_4\text{Sn}$ ), mixed with a solution of poly (ethylene oxide) (PEO,  $\text{HO}-(\text{CH}_2-\text{CH}_2-\text{O})_n-\text{H}$ ) in chloroform ( $\text{CHCl}_3$ ). The  $\text{C}_{22}\text{H}_{44}\text{O}_4\text{Sn}$  compound was chosen because it is inexpensive, commercially available, neither too toxic nor too harmful to the environment and, most importantly, has appropriate rheological properties, especially when it is mixed with PEO/ $\text{CHCl}_3$  solution for electrospinning [Wang et al, 2005]. The second recipe can further introduce pores to fibres as to enhance their ratio of surface area to volume. Such porous  $\text{SnO}_2$  fibres have electrical properties highly sensitive to their environment [Wang et al, 2004]. Since the precursor solution ( $\text{C}_{22}\text{H}_{44}\text{O}_4\text{Sn} / \text{PEO} / \text{CHCl}_3$ ) contains organic groups and Sn-C and Sn-O bonds that are infrared-active, Fourier-transform infrared (FTIR)

spectroscopy will be an effective way to reveal changes in their structure and atomic bonding. This paper uses FTIR, together with thermogravimetric (TG) and differential thermal (DT) analysis (TGA and DTA) and x-ray diffraction (XRD) to further identify the synthesized fibres and to reveal a series of changes that lead to the conversion of the starting chemicals into the final product of porous ultra-fine SnO<sub>2</sub> fibres. This information will help us to control and tailor the micro/nanostructure, porosity and lattice defects of the final SnO<sub>2</sub> fibres so as to meet different specific application requirements.

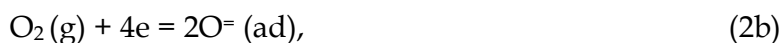
Transparent conductive oxides (TCOs) have received extensive attention because of their important optoelectronic applications such as electrochromic devices, heat mirrors, and transparent electrodes and antireflection coatings in solar cells. Usually such oxides are semiconductors and their transparency is due to their wide band gap [Wang et al, 2007]. Tin oxide or stannic oxide (SnO<sub>2</sub>) is a typical TCO. With a wide band gap of around 3.6eV makes it transparent up to the ultra-violet (UV) light. Although intrinsic stoichiometric single crystal SnO<sub>2</sub> is an insulator, its conductivity can be greatly increased either by impurity doping or by the introduction of oxygen vacancies in its lattice, which donate electrons [Chopra et al, 1983]. Since most optoelectronic, as well as sensing, applications prefer a thin film shape [Chopra et al, 1983; Jarzebski & Marton, 1976], SnO<sub>2</sub> thin films have been synthesized by numerous methods, such as chemical vapor deposition [Davazoglou, 1997], sol-gel [Terrier et al, 1997], spray pyrolysis [Shanti et al, 1999] and polymeric precursor [Giraldi et al, 2006], and their electrical and optical properties have been well characterized [Davazoglou, 1997; Giraldi et al, 2006]. However, for many applications such as a line light source, a fibrous shape is required. Unfortunately, so far only a few methods, namely, thermal decomposition [Xu et al, 2002], laser ablation [Liu et al, 2003], template oxidization [Kolmakov et al, 2003], vapor deposition [Mathur et al, 2005] and electrospinning [Wang et al, 2004,2005], have been developed to fabricate SnO<sub>2</sub> nanofibers or ribbons and their optical properties have been only barely touched [Liu et al, 2004; Dharmaraj et al, 2006] even though such properties characterization is indispensable for their applications. To our knowledge, no report has been made on characterizing their optical band gap, the most important parameter for their optoelectronic applications. The authors of this article have developed two recipes for electrospinning SnO<sub>2</sub> fibers [Wang et al, 2004,2005] and characterized their electrical properties. We investigate their optical and photoconductive properties, with the emphasis on the determination of their optical band gap and conductance response to UV light.

Binary oxide semiconductors have important sensing and optoelectronic applications [Seal & Chukla, 2002; Batzil & Diebold, 2005]. Usually, such oxides have a wide band gap and are good insulators in their undoped and stoichiometric state. However, oxygen vacancies leading to nonstoichiometry can easily be formed in their lattice, donate electrons, and greatly increase their conductivity. Their conductivity is also modulated by species chemisorbed on their surface and the subsequent interaction between the chemisorbed species and the nonstoichiometric oxygen vacancies. We fabricated nanofibers using electrospinning and metallorganics decomposition (MOD) techniques [Wang et al, 2004, 2007]. The conductivity of our synthesized fiber is highly sensitive to its environment, suggesting promising sensing applications. In this letter, we fabricated a gas sensor based on a single electrospun SnO<sub>2</sub> nanofiber and used it to detect moisture, and methanol gases. Although nanowires fabricated in other ways have been used to detect CO, and other gases [Kolmakov et al, 2003], this might be one of the earliest such use using electrospun fibers.

Civilian and industrial safety control, environmental protection and homeland security have stimulated great demand for novel chemical sensors, including gas sensors that can monitor a small amount of toxic, inflammable and/or explosive gases such as hydrogen (H<sub>2</sub>) and carbon monoxide (CO) and odorous components such as O<sub>3</sub> and NO<sub>x</sub>. The core element in a gas sensor is its sensing material. Binary oxide semiconductors constitute a promising family of sensing materials used in gas sensors because they are cost-effective, chemically inert, mechanically hard, and thermally heat-resistant, and therefore can be used in a harsh environment and are reliable over a long term [Williams, 1987; Seal & Chukla, 2002; Batzill & Diebold, 2005]. Electrically, they have a wide band gap and are good insulators if they are pure and stoichiometric. However, point defects, such as oxygen vacancies, can easily form in their lattice leading to non-stoichiometry, and act as donors as depicted below.



Such interactions greatly increase their conductivity. On the other hand, environmental oxygen atoms can be adsorbed on their surface, pick up electrons from the conduction band,



This chemisorption leads to a positively charged layer due to electron depletion immediately below the negatively charged surface and greatly decreasing their conductivity. When the surface is exposed to a reductive gas such as CO, however, the surface-adsorbed O<sup>-</sup> or O<sup>=</sup> ions will react with the reducing gas molecules, release electrons,



Leading to a decrease of the depletion zone, and greatly increasing the conductivity. Such conductivity modulation by surface chemisorbed species and their interaction with the point defects provides a reliable gas detecting mechanism for binary oxide gas sensors [Williams, 1987; Seal & Chukla, 2002; Batzill & Diebold, 2005]

Tin oxide (SnO<sub>2</sub>) sensors represent some of the early-commercialized chemical sensors (the Taguchi sensor [Naoyoshi, 1975]). Usually the SnO<sub>2</sub> sensing element is used in the shape of a thin film [Capone et al, 2001; Mandayo et al, 2003; Korotchenkov et al, 1999] because of its inherent higher surface-to-volume ratio than bulk. A fibrous or ribbon shape is more favorable for surface sensing than bulk and thin films in that it has an even higher surface-to-volume ratio. The ratio can also be increased by the introduction of pores into the SnO<sub>2</sub> thin film [Jin et al, 1998]. So, porous nanofiber/nanoribbon will be doubly favorable for surface sensing. Unfortunately, these had not been synthesized until recently, when we fabricated porous SnO<sub>2</sub> ribbons, with horizontal and vertical dimensions of 100 nm–20 μm and 10–100 nm, respectively, from the metallo-organic precursor dimethyldiiododecanoate tin (C<sub>22</sub>H<sub>44</sub>O<sub>4</sub>Sn) using electrospinning and thermal decomposition techniques [Wang et al, 2004, 2007]. As SnO<sub>2</sub> gas sensors are usually used in atmosphere above room temperature for maximum sensitivity, it is essential to evaluate the electrical conductance (G) of our SnO<sub>2</sub> nanoribbons in analyte gas atmosphere. We also want to find its temperature (T)

dependence between room temperature and its probable elevated operating temperature, which is usually 473 to 773 K [Williams, 1987; Seal & Chukla, 2002; Batzill & Diebold, 2005]. Previous studies on bulk and thin-film SnO<sub>2</sub> has demonstrated that, due to the temperature-sensitive thermodynamics of surface chemisorption/desorption and surface-lattice interaction, conductance is dictated by the temperature to a large extent [Jarzebski & Marton, 1976; Ryzhikov et al, 2003]. In this chapter we briefly explored the electrical conductance of our single electrospun porous nanoribbon and its T-dependence in ambient air, and hopefully paves the way for potential sensing applications.

*Ternary and more complex oxide fibers:* Lead zirconate titanate, Pb (Zr<sub>x</sub>Ti<sub>1-x</sub>) O<sub>3</sub> (PZT), is a well-known ferroelectric material with significant technological importance [Yoshikawa et al, 1995]. PZT fibers have potential for utilization in high performance hydrophones and ultrasonic transducer applications [Yoshikawa et al, 1995]. The author's group synthesized PZT fibers with diameter from 100 nm to 20 μm by means of electrospinning and metallo-organic decomposition [Wang et al, 2002; Wang & Santiago-Aviles, 2004]. Since then, it has been a challenge for us to evaluate their ferro electric properties. Usually, PZT is evaluated as dielectric media in a sandwiched metal/PZT/ metal capacitor [Trolrier-Mckinstry & Murali, 2004]. Such evaluation does not work for a single PZT fiber with diameter less than 10 μm because of its ultra low capacitance. Recently, piezoresponse imaging (PRI) has been developed to probe polarization domains in ferro-electric thin films (including PZT thin film), measure their properties in micro- or nano-scale, and correlate domain polarization and local properties directly with topography and morphology [Birk et al, 1991; Harnagea, 2007]. We will explore the use of such techniques in elucidating PZT properties.

## 2. Experimental details

*Carbon Nanofibers:* The fibers precursor is a commercial polyacrylonitrile (PAN) and N, N-dimethyl formamide (DMF) solution, in a ratio of 600 mg PAN to 10 ml DMF. The solution was deposited on silicon wafers with a 150-nm-thick film of silicon oxide and patterned with 1 X 1 mm<sup>2</sup> gold contact array. A homemade electrospinning setup [Wang et al, 2003], was used to spin single precursor fibers between two isolated gold contacts (Fig. b). The as-spun PAN fibers were pyrolyzed and heat treated at 1273 K for 30 min in a vacuum of 10<sup>-6</sup> torr. The processed fibers were characterized using Raman scattering at room temperature with a green laser (wavelength = 514 nm) as the exciting radiation. The cross-sectional dimensions and area (S) were evaluated using a scanning probe microscopy (SPM) [Wang et al, 2002, 2003].

A two point probe setup was used to continuously monitor the conductance (G) in the temperature range between 300 and 1.9 K, back and forth, without any applied magnetic field. Its resistance (R) was measured from 295 K down to 15 K with a sampling interval around 0.02 K. To suppress the possible heating effect during the measurement, the constant dc current passing through the fiber was kept at 1 μA or below, and the temperature was controlled automatically. Conductance was also measured at 1.9, 3.0, 5.0, and 10.0 K while the applied magnetic field, perpendicular to the fiber, was increased or decreased continuously between -9 and 9 Tesla twice. According to a previous analysis [Rebbouillat et al, 1998], the contact resistance is much less than that of the nanofiber itself. The length L and cross section area S of the fibers were measured using an optical microscope and a scanning probe microscope (SPM) operated in tapping mode. The conductivity was finally determined using  $\sigma = GL/S$ .

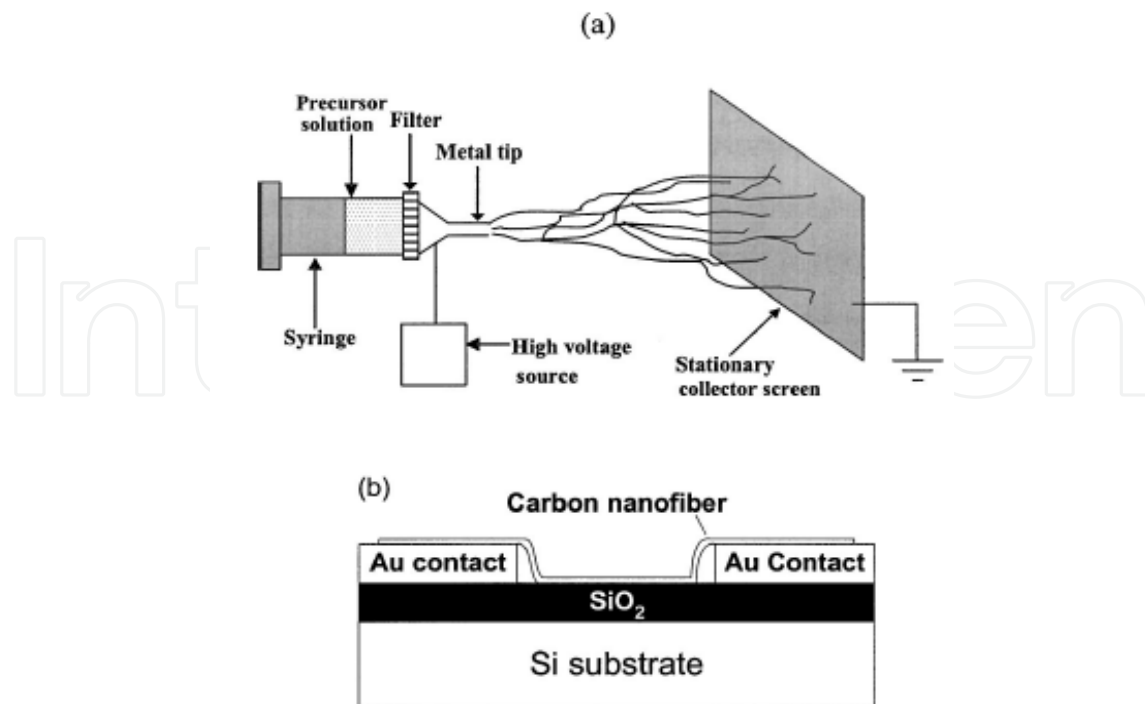


Fig. 1. Schematic of (a) homemade electrospinning setup (b) carbon nanofiber deposited on substrate

**Binary Oxides:** The SnO<sub>2</sub> fiber fabrication process was characterized by a Fourier Transform Infrared Spectrometer, equipped with a semi-demountable liquid cell with rectangular potassium bromide (KBr) windows and a universal attenuated total reflectance (UATR) sampling accessory with composite zinc selenide and diamond crystals on its top plate. The PEO powder was sampled using the UATR; the pristine C<sub>22</sub>H<sub>44</sub>O<sub>4</sub>Sn liquid and the polyethylene oxide/CHCl<sub>3</sub> and precursor (C<sub>22</sub>H<sub>44</sub>O<sub>4</sub>Sn/PEO/CHCl<sub>3</sub>) solutions were sampled using the liquid cell. Since our liquids have strong IR absorption, the spacer was withdrawn from the liquid cell and the liquid samples were pressed between two KBr window plates. The produced film is estimated to be no thicker than 10 μm, thinner than the thinnest spacer commercially available (50 μm). The as-deposited and heat-treated mats were scratched off their substrates, ground into powder and sampled using the UATR. To compensate for the high cutoff wave number (650 cm<sup>-1</sup>) caused by the UATR and Si substrate, the ground powders were then sampled as mulls using the liquid cell with its spacer thickness = 50 μm. Mulls were prepared by dispersing ground powders in the Nujol® (Perkin-Elmer) oil and stirring the mixture electromagnetically until a homogeneous liquid suspension was formed.

**Tin Oxide Nanofibers:** The synthetic procedure, is briefly recounted here to facilitate the analysis of the results in this chapter. Commercially available PEO (molecular weight 900 000) and chloroform were mixed in the ratio of 10 mg PEO/1 ml CHCl<sub>3</sub> and the mixture was stirred using a magnet until the homogeneous solution formed and commercial alkoxide C<sub>22</sub>H<sub>44</sub>O<sub>4</sub>Sn was added to the solution in a volume ratio of 2:1. The new mixture was stirred until it finally became a homogeneous solution with the appropriate viscosity. TGA and DTA on the precursor solution was conducted using platinum (Pt) pans in a simultaneous differential technique module from room temperature to 700 °C at a heating rate of 10 °C

$\text{min}^{-1}$ . The precursor solution, after loading into the pan, was left in the air for its solvent to evaporate until its weight became relatively stable for the thermal analysis to start. Precursor fibres and mats were electrospun using a homemade set-up [84–88] onto thermally oxidized single-crystal silicon wafers with (111) orientation, and heat-treated subsequently in air for 2 h at 200, 300, 400, 500 and 600 °C, respectively. The silicon substrates used were thermally oxidized until their surface oxide thin film had a thickness of around 180 nm. The as-deposited precursor fibres were observed under an optical microscope equipped with a digital camera. The microscope, when in its differential interference contrast (DIC) mode, can form an image which appears distinct and three-dimensional. The fibres after heat treatment were observed under an scanning electron microscope (SEM), operated at an accelerating voltage of 3–5 kV, and characterized using an x-ray diffractometer equipped with a Cu K $\alpha$  x-ray source and a graphite monochromator. Gold contacts of 50  $\mu\text{m}$   $\times$  50  $\mu\text{m}$   $\times$  200 nm with neighboring distance 50  $\mu\text{m}$  were thermally evaporated along one single ribbon using nickel TEM grids as masks, which were fixed by the magnetic force from a flat magnet sheet on the backside of the substrate (figures 2(a) and 2(b)).

Electrical properties of single porous nanoribbons were characterized using a self-assembled system (figure 2(c)) in ambient air with a relative humidity of 90%. The sample was heated using a hot plate. A thermocouple was directly attached to the substrate and used to monitor the temperature. To create a uniform local temperature distribution around the sample, an aluminum case was used to enclose the sample. The sample was heated from 300 to 660 K and, immediately after the measurement at 660K, cooled down to 300K with the measuring temperature isochronally varied around every 10K. At each measuring temperature, the measurement was not performed until the temperature was stable for 5 min. I-V characteristics were measured using the two probe method and a semiconductor characterization system. The measuring voltage was swept cyclically, that is, from 0  $\rightarrow$  1V  $\rightarrow$  -1V  $\rightarrow$  0V with  $\pm 0.01\text{V}$  steps.



Fig. 2. Deposition of Au contacts along a single SnO<sub>2</sub> ribbon using TEM grids as masks: (a) schematics, (b) optical micrograph of resulting sample, (c), schematics of the testing system.

#### *Ternary and more complex oxides:*

### 3. Comments on the experimental results:

*Carbon Nanofibers:* Fig. 3 shows an SEM image of the heat-treated carbon fiber. Its horizontal diameter was measured to be approximately 120 nm. Scanning probe microscopy height image analysis revealed an elliptical cross-sectional profile with approximately the same horizontal diameter of 120 nm, a vertical diameter of only 75 nm [1, Wang et al, 2003], and its area  $S = 7068 \pm 200 \text{ nm}^2$ . The Raman microscattering spectrum shows two strong peaks centered on 1371 and 1588  $\text{cm}^{-1}$ , respectively, indicating disordered and graphitic carbons in the nanofiber. The in-plane graphitic crystallite size  $L_a$  was estimated to be around 2.5 nm [2, Wang et al, 2003].

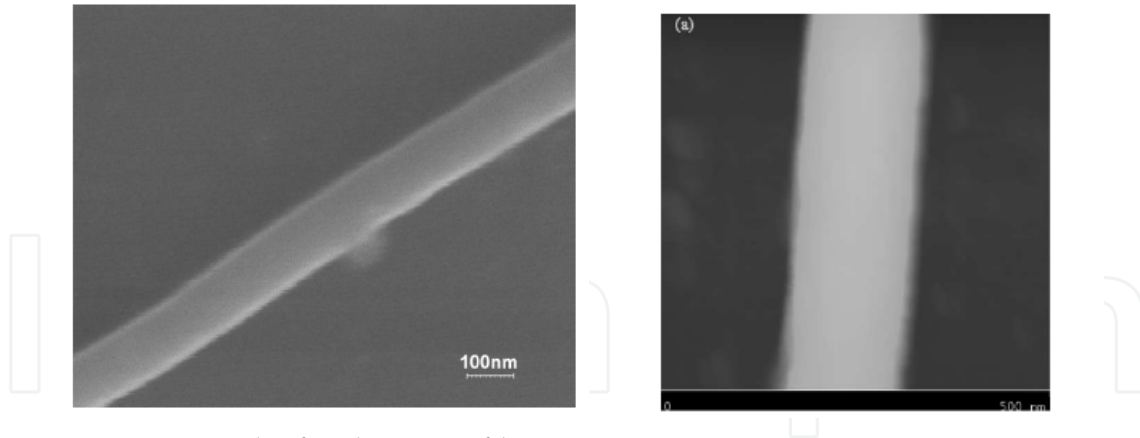


Fig. 3. SEM micrograph of carbon nanofiber

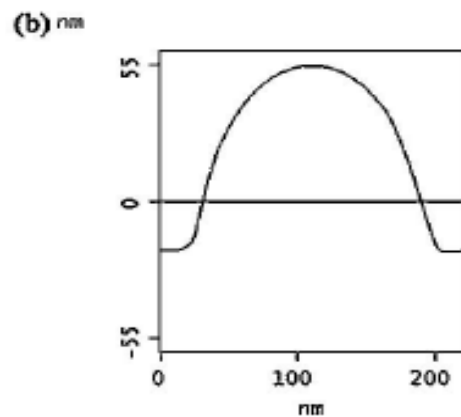


Fig. 4. (a) Scanning probe micrograph of a carbon nanofiber and (b) its average cross-section profile.

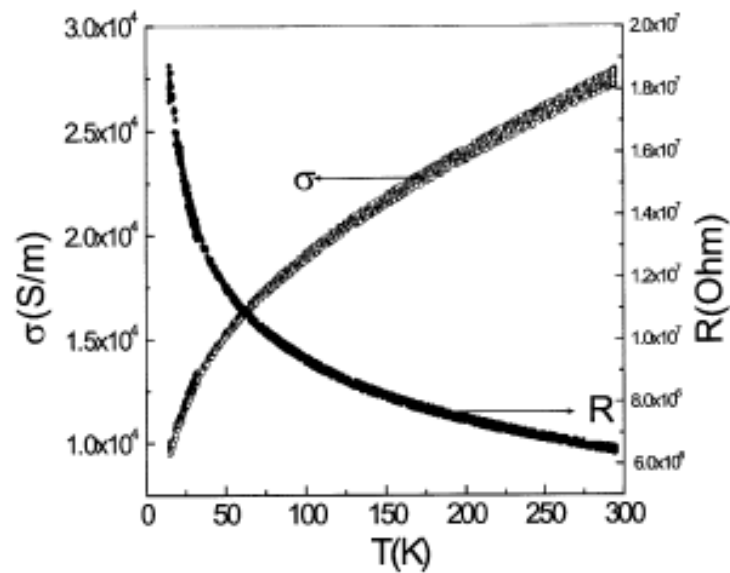


Fig. 5. Temperature dependence of  $R$  and  $\sigma$

The figure above (5), shows a plot of  $R$  and  $\sigma$  versus temperature ( $T$ ) in the range from 15 to 295 K. Note that  $\sigma$  increases monotonically and smoothly from  $1.0 \times 10^4$  S/m at 15 K to  $2.75$

$\times 10^4$  S/m at 295 K, indicating the semiconducting nature of the fiber. Similar temperature dependence of conductivity was also found in carbon microfibers [Spain & Volin, 1983].

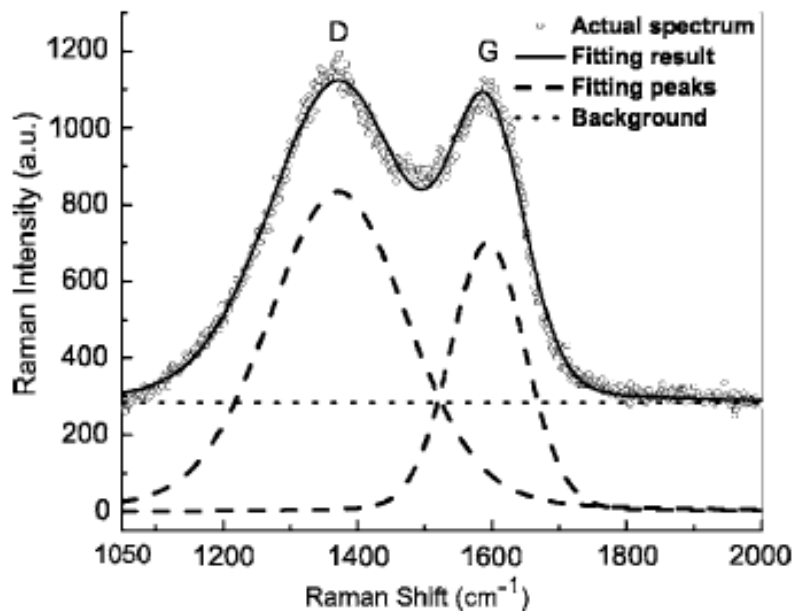


Fig. 6. Raman spectrum of the pyrolyzed fiber

Fig. 6 above, shows the Raman spectrum of the same carbon nanofibers whose G and D peaks, centered at 1371 and 1588  $\text{cm}^{-1}$ , attest to the coexistence of disorder and graphitic carbon in the nanofibers. From the ratio of the integrated intensity of D peak to G peak, the inplane graphitic crystallite size  $L_a$  was estimated to be  $2.47 \pm 0.08$  nm [Mott & Davies, 1979]. The bands were fitted to a Gaussian-Lorentzian shape, with their integrated intensity ratio  $R=2.1$ . Since MC is positive for  $\text{HTT} = 1173$  K, the carrier mobility cannot be measured from the negative parabolic field dependence of MC as in the case of  $\text{HTT} = 1273$  K [146] and the  $n$  value is unknown for the time being. However,  $n$  and  $k_{\text{Fl}}$  values can still be estimated. At room temperature,  $\sigma$  value for  $\text{HTT} = 1173$  K is only half of that for  $\text{HTT} = 1273$  K [Fig. 5(c)]. If the ratio is attributed exclusively to the difference in  $n$ ,  $n$  value for  $\text{HTT} = 1173$  K will be half of that for  $\text{HTT} = 1273$  K [146], i.e.,  $10^{25} \text{ m}^{-3}$ ,  $k_{\text{F}} \approx (3\pi^2 n)^{1/3} \approx 6 \times 10^8 \text{ m}^{-1}$ , and its  $k_{\text{Fl}} \approx k_{\text{F}} L_a$  is 1.2. While the fiber treated at 1273 K between 10 and 200 K, manifesting a WL regime that is not the case for the fiber treated at 1173 K, where the linear relation between  $\ln \sigma(T)$  and  $T^{1/2}$  [Fig. 5(d)] confirms the VRH regime between 300 and 5 K. Although such a relation cannot identify whether the VRH regime is of the Mott type (with  $d=1$ ) or the E-S type, the turbostratic phase structure of our pregraphitic carbon fibers demands  $d=2$  [Mrozowski & Chaberski, 1956], and  $\sigma(T)$  with  $\text{TES} = 187$  K. Using  $\xi \approx L_a \approx 2$  nm, we can estimate  $\epsilon_r \approx 200$ . This value seems reasonable in that it lies between the metallic and insulating limits of  $\epsilon_r \approx \infty$  and  $\epsilon_r \approx 10$ , respectively.

Fig. 7(a) shows the magnetoresistance MR, defined as  $\text{MR} = \rho(B)/\rho(0) - 1$ , and the magnetoconductivity  $\text{MC} = \sigma(B)/\sigma(0) - 1$  of the fibers at temperatures of 1.9, 3.0, 5.0 and 10 K with magnetic field  $B$  from -9 to 9 T. At all four investigated temperatures, the MR is negative. Its magnitude increases with an increase in  $B$  and a decrease in  $T$ . It is noteworthy that  $\text{MR} = -0.75$  at  $T = 1.9$  K and  $B = 9$  T, one of the largest negative magnetoresistance known to the authors. Since  $|\text{MR}|$  is quite large,  $\text{MR} \approx (\text{MC})^{-1}$  is not always valid. The

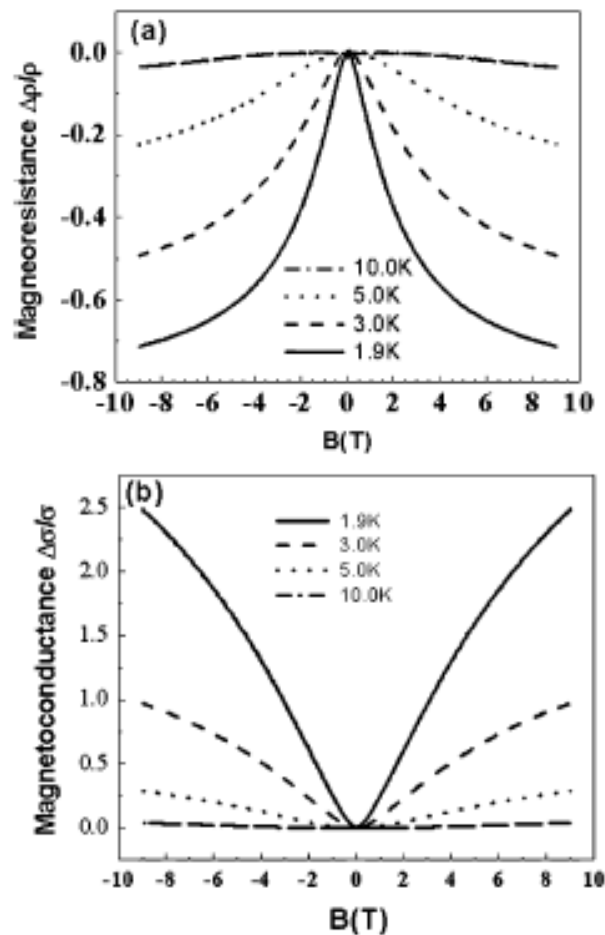


Fig. 7. (a) Large negative magnetoresistance and (b) positive magnetoconductance of carbon fibers with magnetic field from -9 to 9 T.

magnetic field dependence of magnetoresistance for most electronic systems exhibiting 2-D weak localization is relatively easy to understand. In carbon fibers, however the origin is *a priori* not obvious. Bright attributed the origin to the turbostatic nature of the samples, which should have an electronic structure nearly the same as that of 2-D graphite. In the 2-D regime, the correction to the sheet conductance  $G$  produced with the magnetic field  $B$  perpendicular to the plane of the 2-D carrier system is given by the following expression [Bayot et al, 1989, 1990], [Rosenbaum, 1985]:

$$G(B, T) = G_{\infty} + \frac{e^2}{\pi h} \left[ \frac{3}{2} \Psi \left( \frac{1}{2} + \frac{B_2}{B} \right) - \Psi \left( \frac{1}{2} + \frac{B_1}{B} \right) - \frac{1}{2} \Psi \left( \frac{1}{2} + \frac{B_3}{B} \right) \right], \quad (4)$$

$$B_1 = B_0 + B_{s.o.} + B_s,$$

$$B_2 = B_i(T) + \frac{4}{3} B_{s.o.} + \frac{2}{3} B_s,$$

$$B_3 = B_i(T) + 2B_s,$$

$G_{\infty}$  is the sheet conductance at infinite magnetic field, or as calculated in the classical Boltzmann formulation of the transport theory;  $\psi$  is digamma function, and  $B_k$  ( $k=0, I, s, s.o.$ ) represents the characteristic field associated with the scattering mechanism  $\kappa$  standing for elastic scattering (o), inelastic scattering (i), magnetic impurity scattering (s) and spin-orbit coupling (s.o.). Therefore, the magnetoconductance takes the form

$$MC = \eta(T) \left[ \frac{3}{2} \Psi \left( \frac{1}{2} + \frac{B_2}{B} \right) - \Psi \left( \frac{1}{2} + \frac{B_1}{B} \right) - \frac{1}{2} \Psi \left( \frac{1}{2} + \frac{B_3}{B} \right) - \ln \frac{B_2^{3/2}}{B_1 B_3^{1/2}} \right], \quad \text{where } \eta(T) = \frac{e^2}{\pi h G(0, T)}. \quad (5)$$

Given a temperature  $T$ , (5) contains only four unknown parameters:  $\eta(T)$ ,  $B_1$ ,  $B_2$ , and  $B_3$ . They can be derived from a nonlinear fitting. The results show that  $B_2$  and  $B_3$  have very close fitting values. In fact, their difference is less than their respective fitting errors. This indicates that both  $B_{s,o}$  and  $B_s$  are very small, i.e., both magnetic impurity scattering and spin-orbit coupling are very weak. For simplicity, we assume  $B_{s,o} \approx B_s \approx 0$ , and  $B_1 = B_0$ ,  $B_2 = B_3 = B_i(T)$ . Then (5) can be simplified as

$$MC = \eta(T) \left[ \Psi \left( \frac{1}{2} + \frac{B_2}{B} \right) - \Psi \left( \frac{1}{2} + \frac{B_1}{B} \right) - \ln \frac{B_2}{B_1} \right]. \quad (6)$$

Nonlinear curve fitting using (6) and Mathematica software (shown in Fig. 8) showed that  $B_i$  increases with  $T$ , i.e., the inelastic scattering intensifies when the temperature increases.

The temperature dependence of zero field conductivity can be considered in parallel to the modified STB model [Wang & Santiago-Aviles, 2003], which accounts for the conductivity phenomenological, several other models can explain the temperature dependence of the conductivity, namely: 1) 2-D weak localization model: According to the 2-D weak localization model [Lee & Ramakrishnan, 1985; Langer et al, 1996]

$$\sigma(T) = \sigma(0) + \frac{e^2}{2\pi^2 \hbar} \ln \left[ 1 + \left( \frac{T}{T_C(B, \tau_s)} \right)^p \right] \quad (7)$$

where  $\sigma(0)$  and  $T_C(B, \tau_s)$  are two constants. If (7) is used to fit the temperature dependence of the zero field conductivity, we obtain,  $\sigma(0) = 0$ , and  $p = 1.15$  (Fig. 9). The value  $p=1.15$  is in agreement with the previous results of  $p \approx 1.00$  in carbon microfibers [Bayot et al, 1989] and multiwalled carbon nanotube [Langer et al, 1996]. It indicates that the dominating inelastic scattering mechanism is likely to be disorder enhanced electron-electron scattering in 2-D system.

2) Variable range hopping model: This phenomenon occurs in highly disordered materials because the distribution of energy states makes it more favorable to hop to a distant empty state of nearly the appropriate energy than to a nearby empty state that has a much higher energy level. Because of the high resistivity and lack of long-range order of the fiber, one

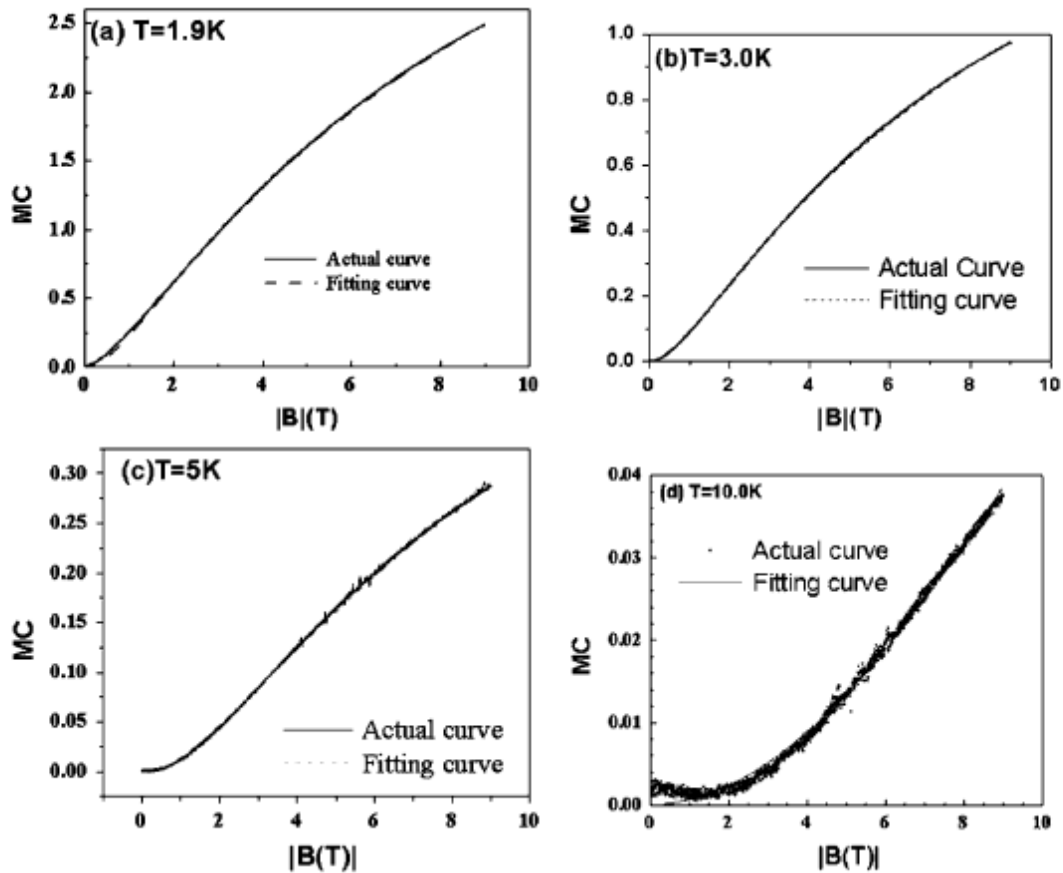


Fig. 8. Comparison of magnetoconductance fitting curves [using (6)] with experimental curves.

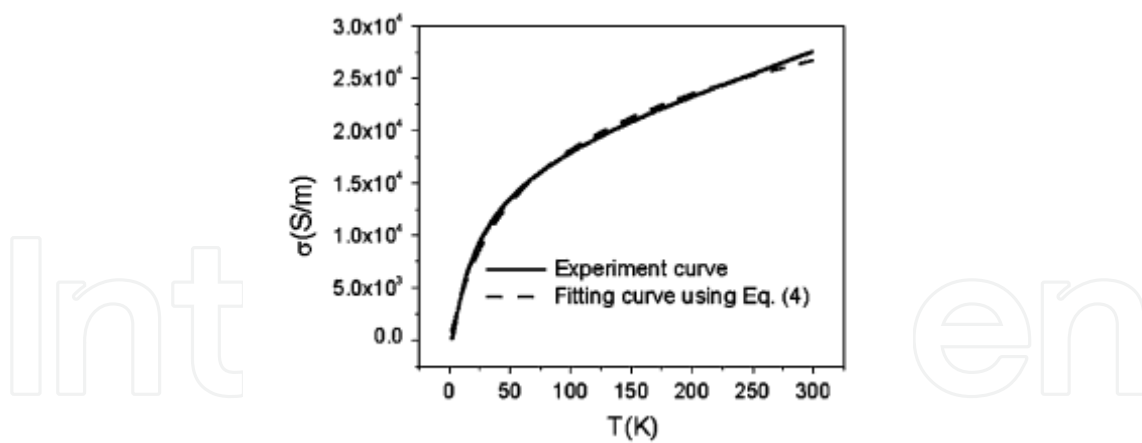


Fig. 9. Fitting of conductivity curve to (7).

would expect that the electrical conduction would result from a hopping mechanism. The dimensionality enters the equation during the summing of the available states. For a  $d$ -dimensional system [Mott & Davies, 1979]

$$\sigma(T) = A \exp \left[ -\frac{B}{T^{1/(d+1)}} \right] \tag{8}$$

where  $d = 1, 2, 3$ , and  $A, B$  are two constants. Since there is controversy about the dimensionality of the carbon fibers with respect to variable range hopping, a good three-parameter fit to all the data was found by least square fitting of the data to (8)(Fig. 11). The fitting results  $d = 0.295$  indicates that the dimensionality of hopping lies between 2 and 3, or that  $d = 2$  and  $d = 3$  coexist.

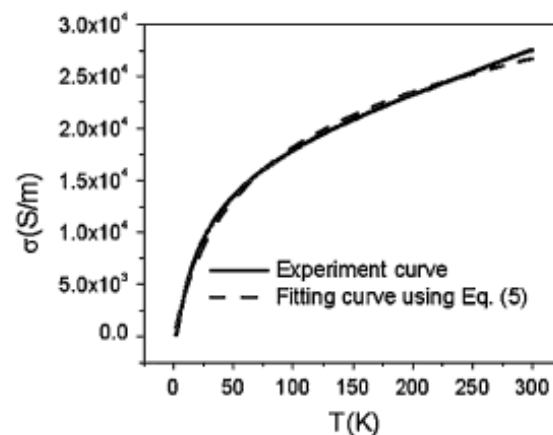


Fig. 10. Fitting of conductivity curve to (5).

Tunneling can be considered as part of transport, the tunneling model was developed for metallic particles imbedded in a highly resistive matrix but the only essential feature of the metallic particles is that the conduction electrons therein are delocalized. As revealed by XRD and Raman spectra, the graphite domains within our carbon nanofibers have a size of 1 to 2 nm [3, Wang et al, 2003]. Since electrons on the small fully carbonized basic units fit this criterion, it is not unreasonable that the model may apply to the investigated fibers. For dc conduction, electron tunnel between the charging centers imbedded in a highly resistive matrix of totally disordered carbon might be plausible. When the electric field is low, the conduction is ohmic resulting in thermally activated charge carriers hopping to the nearest neighbor-charging center. For high-electric fields, the conduction is highly nonohmic and is the result of field-induced tunneling. The conductivity in this model has the same form as 1-d variable range hopping [Abeles et al, 1975]

$$\sigma(T) = A_1 \exp \left[ -\frac{B_1}{T^{1/2}} \right] \quad (9)$$

Where  $A_1$  and  $B_1$  are two constants. If the  $\sigma(T)$  versus  $T$  curve is fit to (9) [Fig. 11], we obtain  $A_1 = 41172$  S/m,  $B_1 = 7.92617$  K<sup>1/2</sup>. It seems reasonable to try to fit the data to a model in which 3-D variable range hopping and tunneling between domains, in which the electrons are delocalized, coexist. The conductivity for such a case is

$$\sigma(T) = A \exp \left[ -\frac{B}{T^{1/(d+1)}} \right] + A_1 \exp \left[ -\frac{B_1}{T^{1/2}} \right]. \quad (10)$$

Fig. 12 shows the results of fitting the data to (10). The fitting is excellent. The figure also shows the curves for the two components. They indicate that the conduction is mostly undertaken by a tunneling mechanism. It increases the convexly with the temperature, the

hopping mechanism accounting for only a small fraction of the total (its contribution to the conductivity increases concavely with the temperature). As such, the hopping mechanism can be excluded from the main transport mechanism(s) in the investigated carbon fiber.

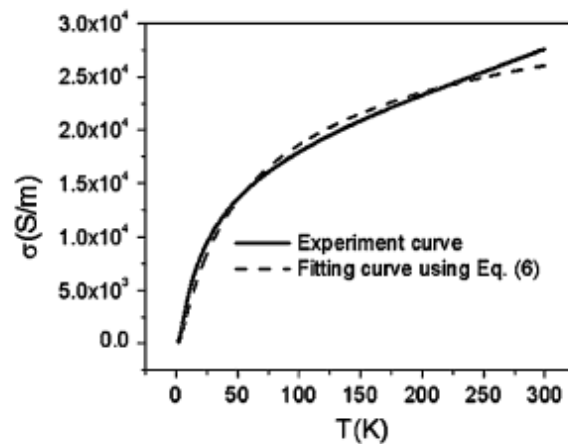


Fig. 11. Fitting of conductivity curve to (9)

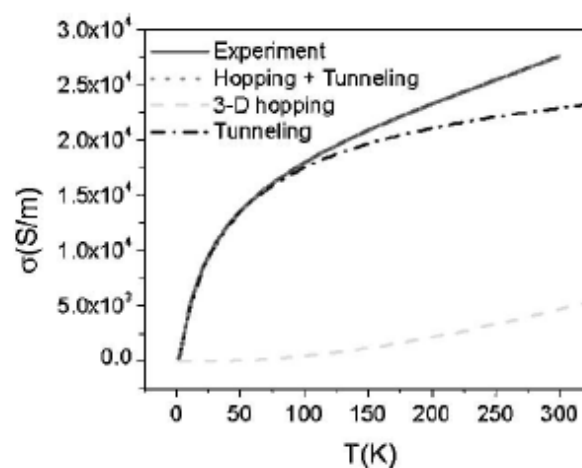


Fig. 12. Fitting of conductivity to (7)

Since both (7) and (9) fit the experimental  $\sigma$  versus  $T$  curve quite well, the fitting alone seems not enough to determine whether the main transport mechanism is 2-D weak localization effect, or the tunneling mechanism. However, the good description of the  $T$ - and  $B$ -dependence of the large MR that can be done using 2-D weak localization effect indicates that the same effect is mainly responsible for the  $T$ -dependence of the conductivity. This harmonizes with the low-electrical field setup during the conductance measurement. The voltage applied between the two conducting pads, separated by a distance of 1 mm, is 0.03-0.6 V. So the average electrical field in the carbon nanofiber between the two pads is 30-600 V/m, not strong enough for the tunneling mechanism to dominate.

*Binary oxides:* Previously we discussed the precursor mixing process for  $\text{SnO}_2$ . Here, Figure 13 shows thermal analysis curves of the precursor solution. As the temperature increases from room temperature, the weight decreases steadily at first and then slows between 100 and 150 °C, beyond which the weight decreases drastically to 5.2% around 270 °C, where the weight-loss rate drops sharply to a very low level until 385 °C. Above this value the weight

remains practically unchanged. The corresponding derivative TG (DTG) curve also indicates three temperature regions in term of the weight loss, peaked around 60, 246 and 301 °C, respectively. The DTA curve, on the other hand, reveals two partially overlapping processes with their exothermic effect ranging from 220 °C to 280 °C (peaked around 263 °C) and from 280 °C to 390 °C (peaked around 345 °C), respectively. Combining the results, one can see that the TG, DTG and DT curves point out four distinct temperature regions with their respective overall changes:  $\text{CHCl}_3$  evaporates from room temperature to 100 °C (note that 60 °C is its boiling point in air); PEO and  $\text{C}_{22}\text{H}_{44}\text{O}_4\text{Sn}$  decompose rapidly into an intermediate product between 220 and 300 °C; the intermediate product undergoes a minor weight loss between 300 and 385 °C; and no major chemical reaction occurs with weight change above 400 °C.

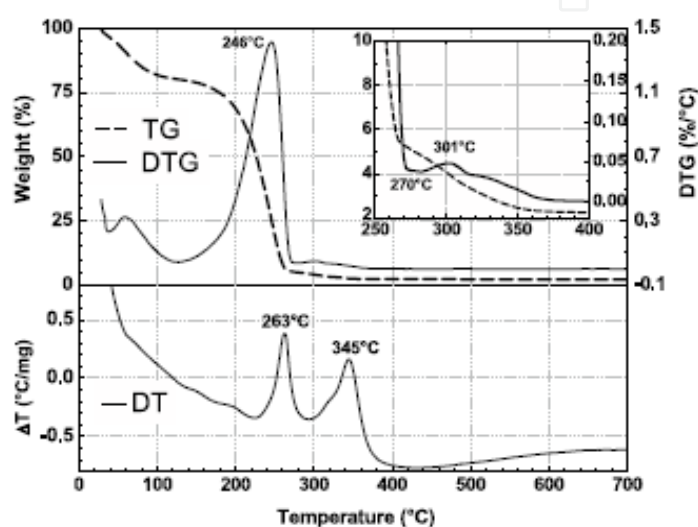


Fig. 13. Thermal analysis (TG, DTG and DT) curves of the precursor solution. The inset highlights TG and DTG curves between 250 and 400 °C

The XRD spectra shown in figure 14 indicate that the samples were amorphous and the 100, 101, 200 and 211 characteristic peaks of the rutile-structured  $\text{SnO}_2$  [JCPDS cards] do not emerge until 400 °C. The peaks become more distinct as the heat treatment temperature rises. Additional peaks indexed to the 220 and 310 planes, indiscernible after the heat treatment at and below 500 °C, became evident at 600 °C although they are not as strong and distinct as the others. Except for the Si (111) peak [JCPDS cards] from the substrate in the spectrum of 500 °C, all peaks are characteristic of rutile-structured  $\text{SnO}_2$ . The multiple diffraction peaks reflect the polycrystalline nature of the sample. Their relative intensity, similar to that in the JCPDF card of rutile-structured  $\text{SnO}_2$ , indicates no obvious texture (preferential orientation) of crystallites within the samples. The combination of thermal analysis and XRD results gives us a clearer picture of the process: while the exothermic process between 220 and 300 °C does not produce any crystallization, the other process, between 300 and 385 °C, results in the incipient rutile lattice. Above 400 °C, the major change is the further development of the incipient lattice, i.e. phase transformation without obvious weight or stoichiometric change. Optical micrographs show precursor fibres of smooth surfaces with indent belts (figures 15(a) and (b)) along their length axis, whose formation mechanism is under investigation. The equal-thickness interference fringes in figure 21(a) clearly indicate that the height/thickness of the precursor fiber varies along the

direction of the horizontal diameter. Optical microscopic observation also revealed that the final  $\text{SnO}_2$  fibres have typical lengths of up to a few millimeters. SEM observation further revealed that the fibres are porous and their diameters range from 100 nm to 40  $\mu\text{m}$  (figures 15(c)-(f)).

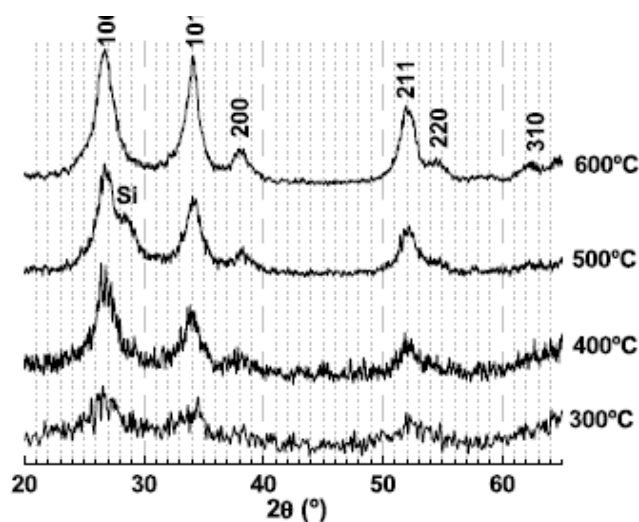


Fig. 14. X-ray diffraction spectra of mat samples heat treated from 300 to 600 °C. The indexes were assigned as the rutile structure of  $\text{SnO}_2$  according to [JCPDS cards]. The extra peak at 500 °C is due to (111) diffraction of the single-crystal Si substrate according to [JCPDS cards]. The mat sample heat treated at 500 °C was not dense and thick enough for the diffracted x-ray by the Si substrate not to be detected.

The most porous regions in the final fibres lie in the indent bands of the precursor fibres. We are investigating how the former evolve from the latter and trying to quantitatively measure the surface area of our porous fibres using the BET or any other pertinent method [Brunauer et al, 1938]. The difficulty of the measurement lies in synthesizing enough of the material to do the isotherms and separating our fibres from their substrates without changing their porous morphology. Figure 15(a) shows FTIR spectra of the starting chemicals PEO,  $\text{CHCl}_3$  and  $\text{C}_{22}\text{H}_{44}\text{O}_4\text{Sn}$  with their major absorption bands tentatively assigned. The assigning for  $\text{CHCl}_3$  was easy as it and its IR spectrum are well known and widely published [Silverstein & Webster, 1998]. The assigning for PEO was helped by [Ratna et al, 2006] and [Deng et al, 2006]. The work for  $\text{C}_{22}\text{H}_{44}\text{O}_4\text{Sn}$  was the most difficult: it is rarely reported and its IR spectrum is unavailable in the literature.

In the FTIR spectrum of the as-deposited precursor mats (figure 16(a)), there is no chloroform absorption bands, indicating a total evaporation of the volatile solvent during the electrospinning. In fact, the as-deposited spectrum is similar to that of pure  $\text{C}_{22}\text{H}_{44}\text{O}_4\text{Sn}$  except for the sharp bands centred around 1553 and 1411  $\text{cm}^{-1}$ . The former 'extra' band was weakened and shifted to 1530  $\text{cm}^{-1}$  by the heat treatment at 200 °C, which, however, did not change other major characteristic bands except for the shift of the bands below 800  $\text{cm}^{-1}$  toward lower wavenumber. Significant changes occur after the heat treatment at 300 °C, where the bands of such organic groups as methyl ( $-\text{CH}_3$ ), methylene ( $-\text{CH}_2$ ), methylidyne ( $-\text{CH}$ ), carbonyl ( $-\text{C}=\text{O}$ ) and hydroxyl ( $-\text{O}-\text{H}$ ) almost disappear (figure 16(b)), suggesting their decomposition. Meanwhile, there appears a band around 760–730  $\text{cm}^{-1}$ , which can be attributed to the asymmetric Sn–O–Sn stretching [Almaric-Popescu, 2001], and the Sn–C band merges with the band previously around 634  $\text{cm}^{-1}$  into a broad band centred around

540  $\text{cm}^{-1}$ . These changes are accompanied by an overall exothermic effect and drastic weight loss (figure 13), characteristic of thermal decomposition of organics. All these strongly suggest that the organic groups in the precursor fibres were thermally decomposed between 200 and 300  $^{\circ}\text{C}$ . The product of the thermal decomposition, as previously revealed by its XRD spectrum, is an amorphous, rather than rutile-structured,  $\text{SnO}_2$ .

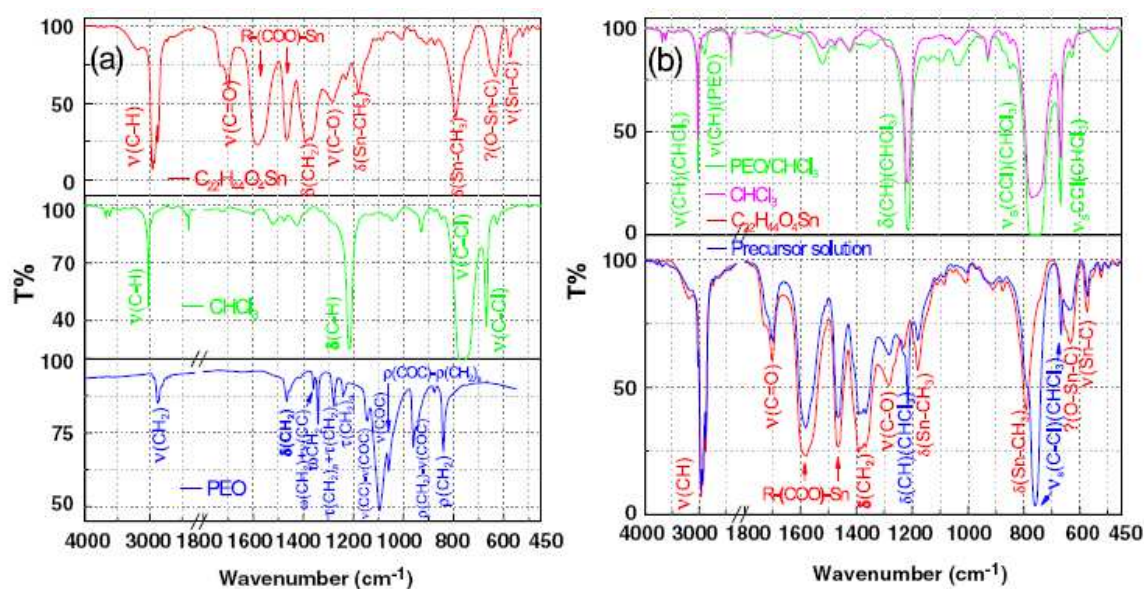


Fig. 15. The FTIR spectra and their absorption band assignment of the starting (a) chemicals: PEO,  $\text{CHCl}_3$  and  $\text{C}_{22}\text{H}_{44}\text{O}_4\text{Sn}$ , and (b) solutions: PEO/ $\text{CHCl}_3$  and  $\text{C}_{22}\text{H}_{44}\text{O}_4\text{Sn}/\text{PEO}/\text{CHCl}_3$ . The  $\text{C}_{22}\text{H}_{44}\text{O}_4\text{Sn}$  bands were tentatively assigned with the help of neodecanoic acid and tetramethyltin spectra; its band around 634  $\text{cm}^{-1}$  may be due to the O-Sn-C bridging. The spectrum of the PEO/ $\text{CHCl}_3$  solution is mainly that of  $\text{CHCl}_3$  except for the weak C-H stretching band around 2976  $\text{cm}^{-1}$ , which is from PEO. The  $\text{C}_{22}\text{H}_{44}\text{O}_4\text{Sn}/\text{PEO}/\text{CHCl}_3$  precursor solution spectrum, however, is mainly the superposition of those of PEO/ $\text{CHCl}_3$  and  $\text{C}_{22}\text{H}_{44}\text{O}_4\text{Sn}$ . Fortunately, we found IR spectra of neodecanoic acid ( $\text{C}_9\text{H}_{19}\text{COOH}$ ) [Ratna et al, 2006] and tetramethyltin ( $(\text{CH}_3)_4\text{Sn}$ ) [Japanese spectral data base], which have the same major groups and structural chains as  $\text{C}_{22}\text{H}_{44}\text{O}_4\text{Sn}$ . The major bands in the two spectra, tentatively assigned with the help of [Kuag, 2002; Fiaz et al, 2002; Hori et al, 1986; Jing et al, 1995], are also predominant in the  $\text{C}_{22}\text{H}_{44}\text{O}_4\text{Sn}$  spectrum except for the band around 634  $\text{cm}^{-1}$ , which may reflect the bridging of O-Sn-C (figure 16(a)). Note that the band around 574  $\text{cm}^{-1}$  is assigned to the Sn-C stretching [Kuag, 2002; Fiaz et al, 2002; Hori et al, 1986; Jing et al, 1995], those around 792 and 1180  $\text{cm}^{-1}$  are assigned to the Sn- $\text{CH}_3$  bending and that around 1580  $\text{cm}^{-1}$  is assigned to R-(COO)-Sn [Hori et al, 1986]. The assignments are listed in table 1. The major IR absorption bands of the PEO/ $\text{CHCl}_3$  solution mainly come from  $\text{CHCl}_3$  except for the C-H stretching ( $\nu\text{C-H}$ ) band around 2890  $\text{cm}^{-1}$ , characteristic of the C-H stretching in the chain of  $\text{HO}-[\text{CH}_2-\text{CH}_2-\text{O}]_n-\text{H}$ . The FTIR spectrum of the precursor solution, however, appears to be the combination of  $\text{C}_{22}\text{H}_{44}\text{O}_4\text{Sn}$  and the PEO/ $\text{CHCl}_3$  spectra. The C-Cl band of  $\text{CHCl}_3$  between 840 and 700  $\text{cm}^{-1}$  merges with the Sn- $\text{CH}_3$  band of  $\text{C}_{22}\text{H}_{44}\text{O}_4\text{Sn}$  between 850 and 700  $\text{cm}^{-1}$  to form a broader band of the precursor solution from 850 to 700  $\text{cm}^{-1}$ , peaked at 760  $\text{cm}^{-1}$  and with a shoulder at 780  $\text{cm}^{-1}$  (figure 16(b)). It is noteworthy that many bands overlap or combined with other bands and their assignments may not be unique. However, that will not affect our later discussion about general chemical changes during the synthetic process.

PEO		$C_{22}H_{44}O_4Sn$	
Band position ( $cm^{-1}$ )	Assignments	Band position ( $cm^{-1}$ )	Assignments
3000–2750	$\nu(CH_2)_a$	2960	$\nu(CH_3)_a$
2952, 2800, 2739, 2693	$\nu(CH_2)_a$	2935	$\nu(CH_2)_a$
1467	$\delta(CH_2)_a - \delta(CH_2)_a$	2875	$\nu(CH_3)_s$
1359	$\omega(CH_2)_s + \nu(CC)$	1730, 1700	$\nu(C=O)$
1341	$\omega(CH_2)_a$	1580, 1485	R-(COO)-Sn
1280	$\tau(CH_2)_a + \tau(CH_2)_s$	1465, 1390–1360	$\delta(CH_2)$
1242, 1234	$\tau(CH_2)_a$	1280	$\nu(C-O)$
1145	$\nu(CC) - \nu(COC)$	1230	$\tau(C-H)$
1095	$\nu(COC)$	1180	$\delta(Sn-CH_3)$
1060	$\rho(COC) + \rho(CH_2)_s$	793	$\delta(Sn-CH_3)$
960, 946	$\rho(CH_2)_s - \nu(COC)_a$	634	?(unassigned)
840	$\rho(CH_2)_a$	574	$\nu(Sn-C)$

Table 1. Infrared band assignments for PEO and  $C_{22}H_{44}O_4Sn$ . (Note:  $\delta$  bending;  $\omega$  wagging;  $\nu$  stretching;  $\rho$  rocking;  $\tau$  twisting; a anti-symmetric; and s symmetric; signs + and - denote phase relations of coupled coordinates.)

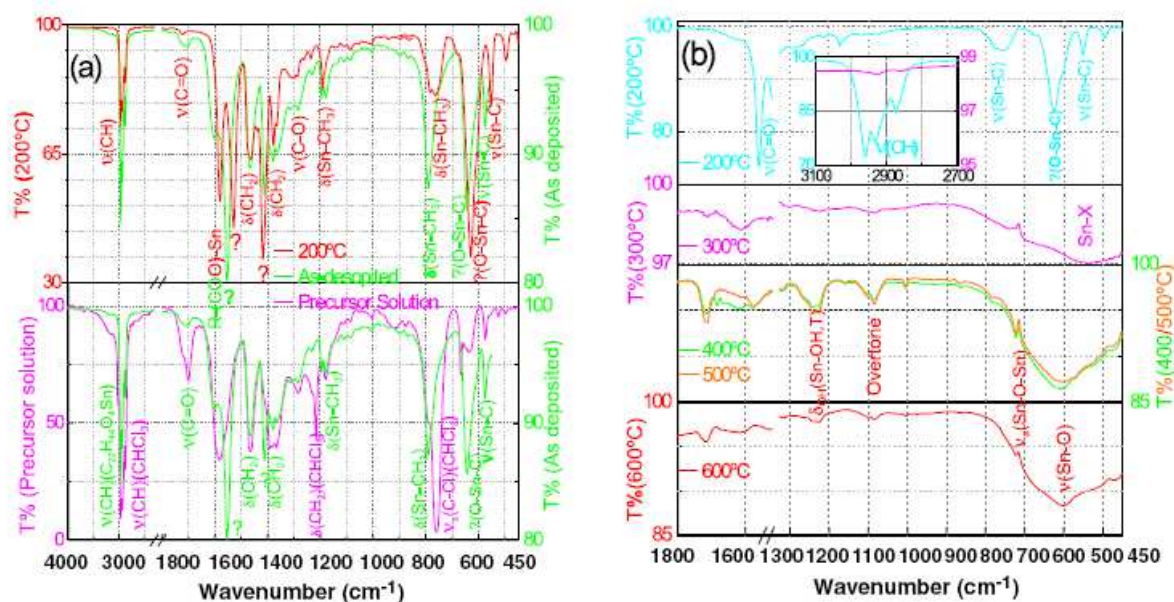


Fig. 16. The FTIR spectra and their absorption band assignment of the precursor solution PEO,  $CHCl_3$  and  $C_{22}H_{44}O_4Sn$ , and mats as-deposited and heat-treated at temperatures between 200 and 600°C. Note that the  $CHCl_3$  bands disappeared immediately after the electrospinning. Bands of other organic groups survive the heat treatment at 200 °C and mostly disappear by the heat treatment at 300 °C, above which spectra do not vary so sensitively with the heat-treating temperature. The inset highlights the disappearance of the C-H stretching band between 3100 and 2700  $cm^{-1}$  of the mats heat-treated at 200 and 300 °C.

FTIR spectra (Figure 17(a)) show that organic groups in the precursor fibers decompose mostly between 200°C and 300°C, and transforms into incipient polycrystalline rutile structure around 400°C. On the other hand, the fibers were transparent from near IR

(wavelength 1100nm) to its UV absorption edge. The edge shifts toward the longer wavelength when HTT increases from 100°C to 300°C, above which the shift is not apparent (Figure 17(b)).

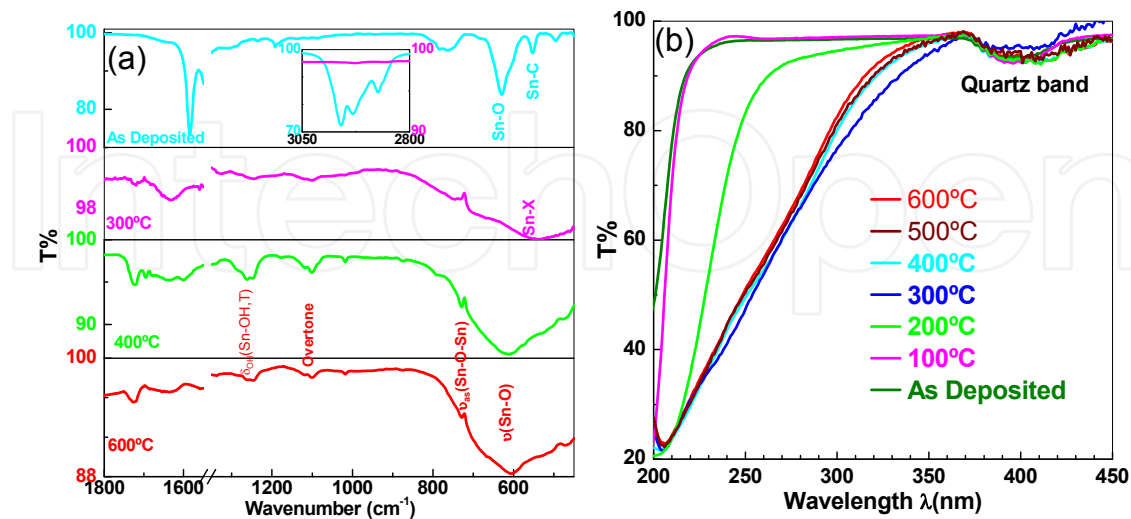


Fig. 17. (a) FTIR and (b) UV/VIS spectra of as-deposited and heat-treated fibers

It is well accepted that the band gap is direct in the rutile-structured  $\text{SnO}_2$  [Chopra et al, 1983]. If direct transition is allowed at zero momentum, the optical absorption coefficient  $\alpha$  follows, on the long-wave limit,

$$\alpha(E) = [A(E - E_g)]^{1/2}, \quad (11a)$$

or

$$[\alpha(E)]^2 = A(E - E_g), \quad (11b)$$

as a function of photon energy ( $E$ ), where  $E_g$  is the optical band gap and  $A$  is a constant [Bardeen et al, 1956]. Since  $\alpha$  and transmittance  $T$  are correlated as

$$T = e^{-\alpha L}, \quad (12a)$$

or

$$\alpha = -(\ln T) / L, \quad (12b)$$

where  $L$  is thickness of sample, we have

$$(\ln T)^2 = AL^2(E - E_g), \quad (13)$$

Heat treating temperature (°C)	300°C	400°C	500°C	600°C
Optical band gap $E_g$ (eV)	3.985~0.004	3.997~0.001	3.952~0.002	4.087~0.002

Table 2. Optical band gap determined from UV absorption edge

which predicts a linear relation between  $(\ln T)^2$  and  $E$ . Such a linear relation is confirmed in the photon energy range of 4.3-5.2eV), and its extrapolation to the  $E$ -axis gives us  $E_g$  values

for different Heat treatment temperatures (Table 2). Overall, the  $E_g$  value increases with HTT but the variation is very small. The values lie within the reported range of 3.8-4.2 eV for SnO<sub>2</sub> thin film using the same method [Terrier et al, 1997; Shanti et al, 1999], and is higher than the better accepted electrical band gap ( $E_{g0}$ ) of stoichiometric single crystal SnO<sub>2</sub>. The possible reasons for the difference include the quantum confinement caused by the porosity [Lehemann & Gosele, 1991] and the Burstein-Moss effect [Burnstein, 1954; Moss, 1954 ] (or the free carrier concentration [Ye et al, 2005]), as well as the defect effect [Terrier et al, 1997]. It is noteworthy that, curves of  $\alpha_i$  ( $i=1/2, 1$ ) and  $(\alpha E)^j$  ( $j=1/2, 1$  and  $2$ ) vs  $E$  have also been linearly fitted and extrapolated to obtain optical  $E_g$ . Such ways of data processing sometimes result in approximately the same  $E_g$  values as those listed in Table I, or values closer to the  $E_{g0}$  value. However, they lack of convincing physical grounds in our case, and their results are not presented here. The four-probe measurement shows that the conductance ( $G$ ) of fibers is insensitive to the visible light, which is consistent with its transparency in the visible light range. However,  $G$  is sensitive to UV light (Figure 19). Upon the UV illumination,  $G$  increases sharply and then asymptotically to its steady value by 58% (the on-to-off ratio is 1.58); when the UV light is turned off,  $G$  decreases asymptotically by 32% (the on-to-off ratio is 1.32) to its new steady values. The 90%- rise and fall times of the conductance are 89 and 119 seconds, respectively. The high optical band gap and photoconductance imply promising optoelectronic applications of the nanofibers. The relatively long response times are attributed to the surface adsorption and desorption processes triggered by the generation and recombination of photo electron-hole pairs. As the experiment was conducted in the air, various species had been adsorbed on the fiber surface and their adsorption had been in equilibrium [Jarzebski & Marton, 1976].

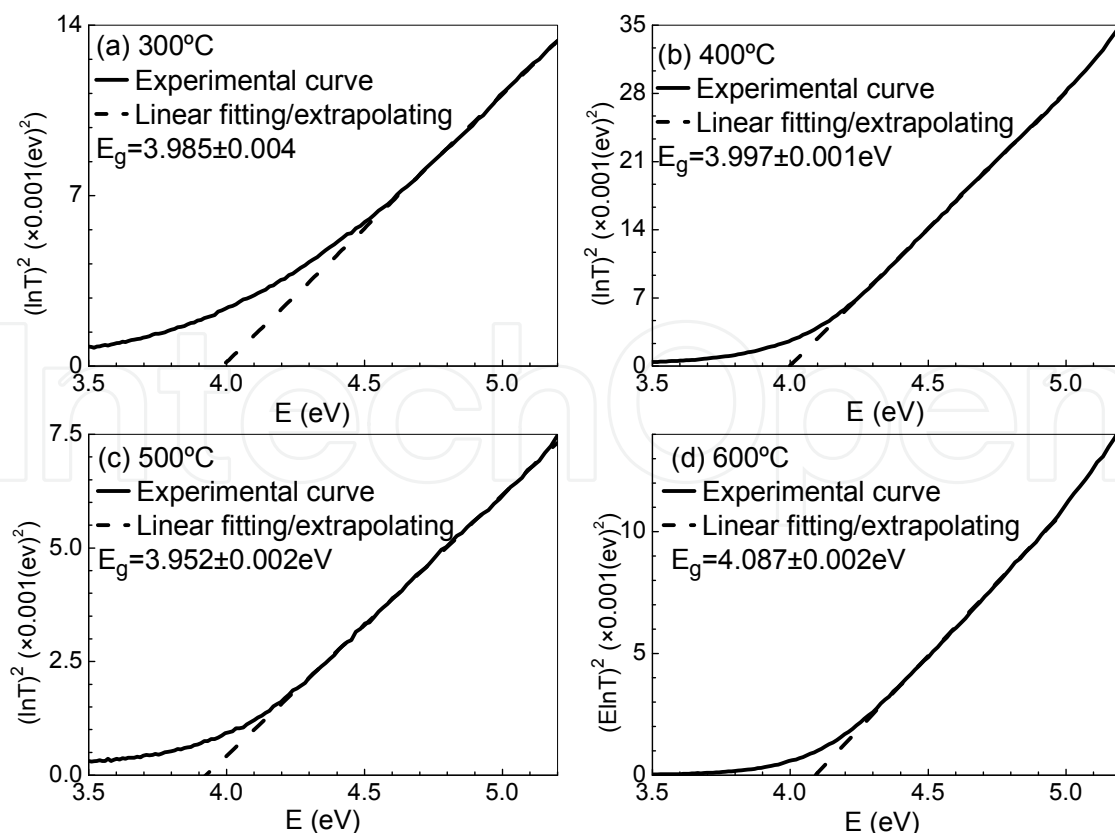


Fig. 18. Determination of optical band gap  $E_g$  from the UV absorption edge.

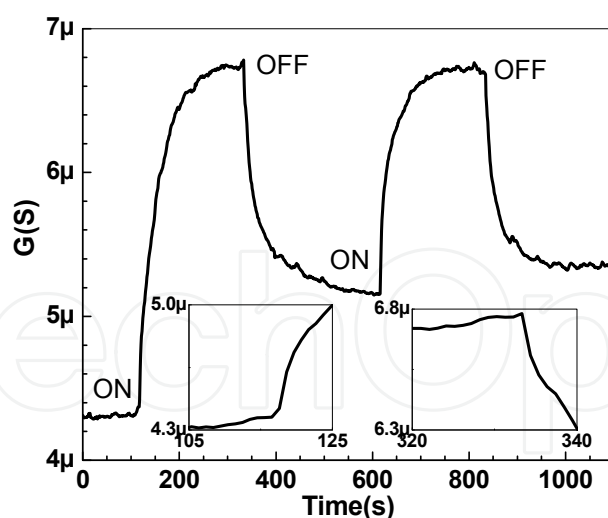


Fig. 19. Transient conductance responses to 254 nm UV light.

The UV-generated electron-hole pairs disturb equilibrium and species are adsorbed or desorbed to attain a new steady surface state. When the UV light is off, the photo electrons and holes recombine with each other, species were adsorbed or desorbed to return to the equilibrium. Since the processes involve surface migration and diffusion of species, the overall stabilization takes time. It is also interesting that  $G$  does not return to its initial value after the first UV on-and-off cycle, implying an irreversible surface change by the UV illumination. However,  $G$  returns to its starting value on the second cycle.

The sensor's typical time response, Fig.20, show the turn-on and off of gases with their main response parameters listed in Table 3. Upon exposure to the nitrogen carrier gas at a higher flow rate, the sensor showed a higher relative conductance ( $G$ ) change and shorter response times, defined as the times it takes  $G$  to change by 90% of the measured change. Such response is reasonable in that a higher flow rate generates a higher moisture concentration in the chamber, accumulates and ventilates it in a shorter time. In fact, the measured response times are those of the whole testing system, and are affected not only by the sensor's intrinsic response time but also by gas generation, transport and venting times. A higher flow rate decreases the latter three times. Additionally,  $G$  increased after the first

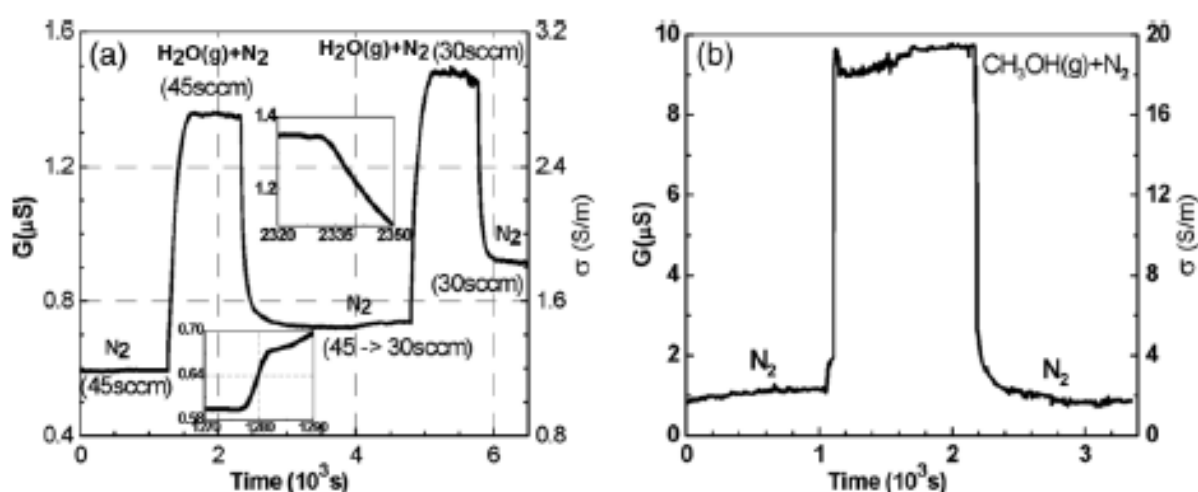


Fig. 20. Response of the sensor to (a) moisture and (b) methanol gas.

exposure to the moisture, suggesting a not totally reversible change (such as adsorption) during that exposure. This may have contributed to the higher G level during the second exposure than during the first.

Such response times, although close to the lower limit of the response time range of sensors based on thin films [Seal & Chukla, 2002], are still dictated by surface adsorption and desorption processes, which, after triggered by the introduction and exhaustion of reducing or oxidizing analytes, involve atomic diffusion and surface species migration

Analyte Gas	N <sub>2</sub> flow rate (sccm)	G(high)/G(low) – 1		90% Response time (s)	
		Rise	Fall	Rise	Fall
CH <sub>3</sub> OH	45	845%	845%	38	10
H <sub>2</sub> O	45	229%	88%	108	150
H <sub>2</sub> O	30	105%	62%	218	187

Table 3. Main response characteristics of the sensor

With the same flow rate of 45 sccm, and increased G by 229% and 845%, respectively. The rise and fall times are 108 and 150 s for water vapor, and 38 and 10 s for ethanol, respectively. The higher relative G change and the shorter response times with do not necessarily mean higher sensitivity to than to since their concentration in the chamber could not be measured. It could, at least partially, be attributed to the higher volatility of , which may have accumulated a higher concentration in the chamber within a shorter time. The effect is consistent with that of the flow rate on the sensor's responses to moisture. Although the sensor's response times are not exactly the same as the measured system response times, they cannot be much less than the latter and are expected to be several to tens of seconds.

All measured I-V characteristics are linear, as typically shown in figure 21(a), and their linear slope (conductance) varies with the measuring temperature as shown in figure 21(b). Apparently both the heating and cooling curves show that G increases slowly with T until 420–480 K, and rises sharply beyond that T range. A careful look into the curves (see the inset in figure 21(b)), however, finds noteworthy differences between the heating and cooling curves. Whereas G does not increase until 400 K during the heating, it decreases steadily during cooling down to 300 K; at the same temperature from 300 to 580 K, G is higher during the cooling than the heating, and, after the heating and cooling cycle, G returns to a higher value than its initial value. Such differences and hysteresis strongly

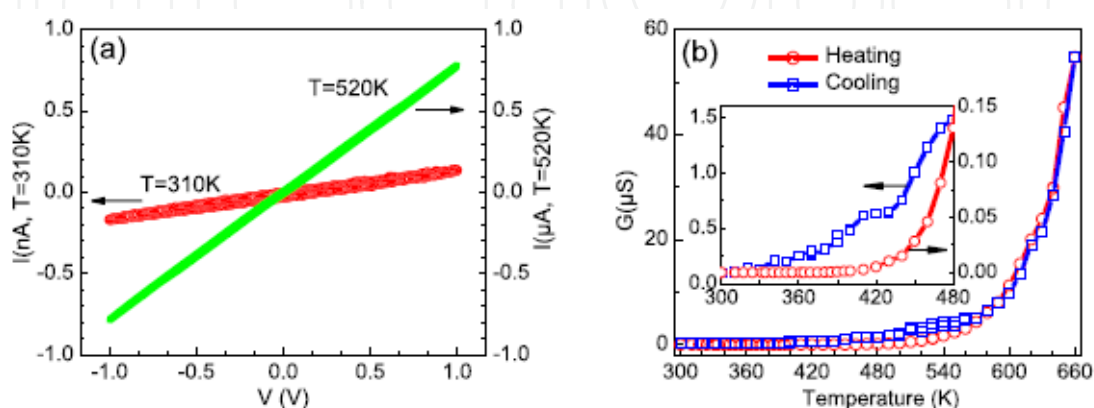


Fig. 21. (a) I-V characteristics and (b) temperature dependence of the conductance

suggest irreversible changes during the cycle, as is the case in SnO<sub>2</sub> thin films [Williams, 1987; Chopra et al, 1983; Jarzebski & Marton, 1976; Ryzhikov et al, 2003]

To look into the mechanism that controls the behaviors shown in figure 21(b), ln G is plotted against 1/T in figure 22(a), where the hysteresis between 300 and 570 K is more obvious. Moreover, during heating from 380 to 660 K, cooling from 660 to 570 K, and cooling from 570 to 300 K, there exist Arrhenius type relations

$$\ln G = \ln G_0 - \Delta E/kT, \quad (14)$$

where k, G<sub>0</sub> and ΔE are the Boltzmann constant, the pre-exponential factor, and the thermal activation energy, respectively, and their fitting values are listed in table 4.

Temperature range (K)	300–380	380–570	570–660
Heating	Non-Arrhenius relation	$\Delta E = 0.918 \pm 0.004$ eV,	
Cooling	$\Delta E = 0.259 \pm 0.006$ eV, $G_0 = 569 \pm 7$	$G_0 = (9.2 \pm 0.2) \times 10^{-4}$	

Table 4. Fitting values for thermal activation energy ΔE and pre-exponential factor G<sub>0</sub>.

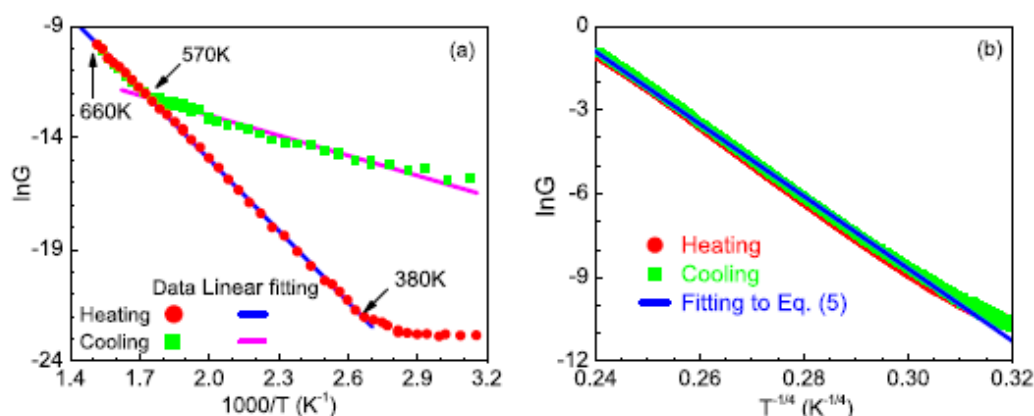


Fig. 22. (a) Arrhenius relation in air and (b) VRH relation in vacuum

For comparison, the T-dependence of conductance in a similar SnO<sub>2</sub> nanoribbon between 300 and 90 K in a vacuum is shown in figure 22(b). Obviously, there is almost no G hysteresis in a vacuum. Although figures 22(a) and (b) correspond to different temperature ranges, their trends around 300 K are comparable. While G is not sensitive to T in air during cooling, σ or equivalently G in vacuum strongly depends on T according to the mechanism of variable-range hopping (VRH) in three dimensions,

$$\ln \sigma(T) = \ln \sigma_0 - (T_0/T)^{1/4}, \quad (15)$$

where σ<sub>0</sub> and T<sub>0</sub> are constants. The comparison clearly indicates that G was controlled by surface-related processes during the heating in air. In fact, the weak G hysteresis in figure 22(b) may be attributed to the partially reversible adsorption and desorption of residual gases in the chamber whose vacuum was only 10<sup>-3</sup> Torr. A similar bifurcate linear ln G versus 1/T relation also exists in SnO<sub>2</sub> thin films and has been attributed to adsorption and desorption of multiple kinds of molecules and species on SnO<sub>2</sub> surface [Williams, 1987; Chopra et al, 1983; Jarzebski & Marton, 1976; Ryzhikov et al, 2003]. However, the specific temperature ranges and ΔE values for SnO<sub>2</sub> thin films differ from our results. The difference

is due to themorphology, impurities and non-stoichiometric defects in  $\text{SnO}_2$ , resulting from different preparation methods and conditions, as well as in the testing environment and procedures. Since our measurement was conducted in air with a relatively high humidity, the effect of moisture, in addition to oxygen, must be taken into account. Although the detailed intermediate mechanism is still ambiguous and perhaps controversial, it is accepted that moisture, after chemisorption and reaction, donates electrons and increases  $G$  like a reducing gas following the overall path



where  $S$  stands for the  $\text{SnO}_2$  surface. Note that moisture and oxygen have opposite effects on  $G$  and their adsorption and desorption dynamics are different. It is plausible that the surface-chemisorbed  $\text{H}_2\text{O}$  molecules are desorbed during heating from 300 to 380 K and that the desorption consumes conducting electrons (according to the reverse of equation (23)). However, the consumption is compensated for by the increase of bulk conducting electron concentration due to  $T$  rises, and the overall  $G$  is not sensitive to the temperature in this range. At around 380 K, oxygen starts to be desorbed from the surface and the desorption contributes to the overall net  $G$  increase as described by the Arrhenius relation equation (21). Upon cooling, oxygen is adsorbed reversibly and  $G$  follows the same Arrhenius relation until 570 K, where the  $\text{H}_2\text{O}$  molecules start to be additionally adsorbed, slowing down the overall  $G$  decreasing rate and reducing the activation energy  $\Delta E$  because of its opposite effect to that of oxygen adsorption. The  $G$  versus  $T$  hysteresis seems to be a consequence of the partial replacing of the adsorbed oxygen by moisture on the  $\text{SnO}_2$  surface after the heating and cooling cycle. Such irreversible replacement in turn can be attributed to the numerous pores within the ribbon, whose capillary effects additionally restrict adsorption, desorption, diffusion, and evaporation around and inside them [Ryzhikov et al, 2003].

The SEM and SPM analysis indicates that the  $\text{SnCl}_4$  precursor led to better results in terms of uniformity/continuity of the fibers. Figure 23 shows the XRD spectra for fibers electrospun using the  $\text{SnCl}_4$  precursor. After sintering at 400 °C, 110, 101 and 211 XRD peaks of rutile structure  $\text{SnO}_2$  appear, indicating the formation of its recipient lattice. These peaks become more distinct and an additional 200, 220 and 310 peaks showed up after sintering at 600 °C,

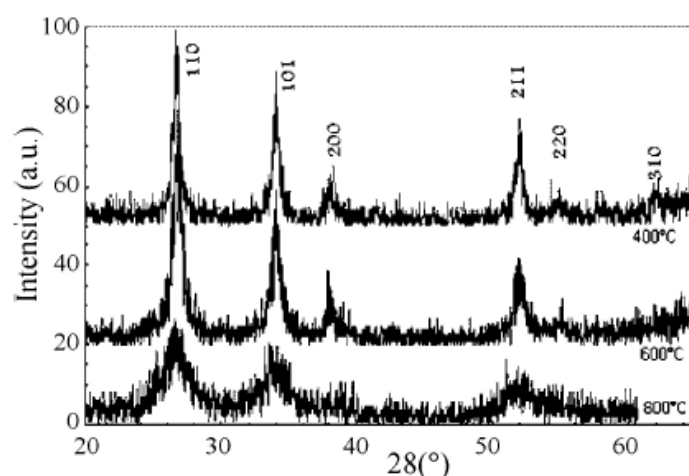
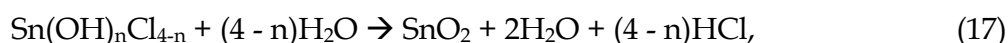


Fig. 23. XRD spectra for  $\text{SnCl}_4$ -based fibers at different temperatures.

indicating the development of a more integral rutile lattice between 400 °C and 600 °C. Up to 800 °C, all peaks are still identified as SnO<sub>2</sub> peaks, suggesting the following overall chemical reactions:



and  $n = 0, 1, 2, 3, 4$ .

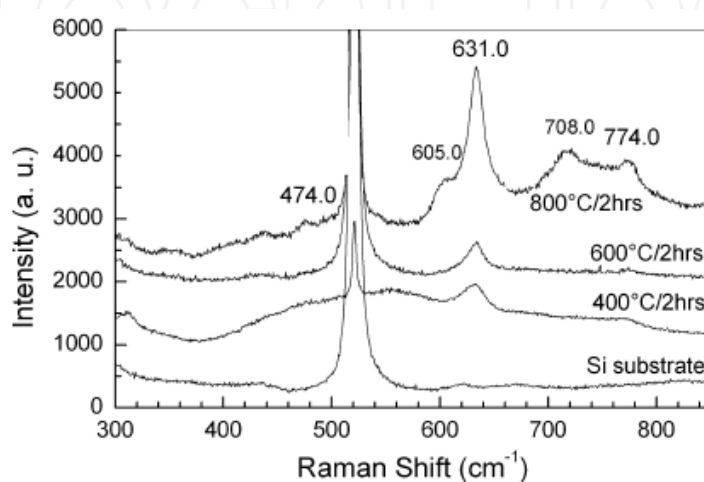


Fig. 24. Raman micro-spectra of Si substrate and SnCl<sub>4</sub>-based mats sintered at different temperatures.

For sintering temperatures of 400, 600 and 800 °C, the relative intensities of the diffraction peaks are consistent with those reported in Ref. [JCPDS cards]. Typical Raman micro-scattering spectra are presented in Fig. 24. After sintering at 400°C, a peak around 631cm<sup>-1</sup> shows up, whereas another weak peak centered around 774cm<sup>-1</sup> begins to appear. The two peaks become more distinct after sintering between 600 and 800°C, whereas the third peak appears around 474 cm<sup>-1</sup> after sintering at 800°C. The SnO<sub>2</sub> rutile structure belongs to the space group P4<sub>2</sub>/mnm [Scott, 1970]. Using X-ray photoelectron spectroscopy atomic sensitivity factors, the relative atomic concentrations of Sn, O, C and Cl were analyzed semi-quantitatively and their dependence on the sintering temperature is shown in Fig. 25.

Upon sintering at 400°C, Cl almost disappears; C concentration decreases sharply from 36.4% to 5-8%, whereas O concentration increases to more than 50%, and Sn concentration increases to 38%. The drastic decrease of carbon concentration and the regular shift of the XPS Cls peak caused by sintering suggest that the carbon is a residual element rather than an adventitious extrinsic impurity.

*Ternary and more complex oxides:* For the PZT Perovskite, the starting metallo-organics were still zirconium n-propoxide (dissolved in free alcohol), titanium isopropoxide, and lead 2-ethylhexanoate. The synthesis process was the same as above, except for the two refinements: (1) The viscosity was increased by reducing the fraction of xylene; (2) A syringe filter was added to the tip. Single crystal silicon wafers, coated or uncoated with a 150 nm-thick platinum film, were used as substrates. The as-electrospun precursor fibers or mats were sintered in air for two hours at 300, 400, 500, 600, 700, 800, and 850°C, respectively. Samples of the thick precursor solution, uniformly spread over a silicon wafer by spin-coating, as-electrospun and as-sintered fibers or mats were characterized using a Rigaku x-

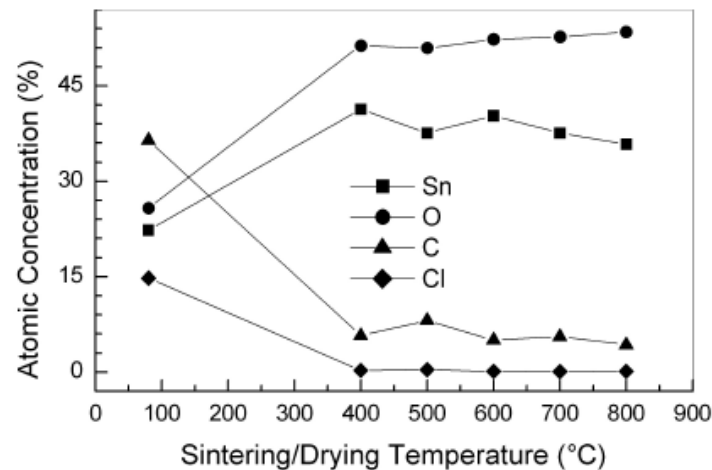


Fig. 25. Sintering temperature dependence of the atomic concentration of SnCl<sub>4</sub>-based fibers.

ray diffractometer and a JEOL JSM-6300FV scanning electron microscope, equipped with an energy dispersion spectroscopy (EDS) attachment. The precursor solution and the mats were additionally characterized using an FTIR spectrometer. While the transmittance spectra of the precursor solution were obtained using a liquid cell with spacing of 0.05mm, specular reflectance spectra of mats samples were obtained using a specular reflectance accessory. In latter case, the same substrates, without any deposit and sintered in the same batch with the tested samples, were used for background scanning. The sintered samples were imaged and analyzed by piezoresponse imaging techniques (PRI). This technique is implemented through the combination of scanning probe microscopy and lock-in electrical measurement techniques [Birk et al, 1991; Harnagea, 2007]. It makes use of a sandwiched conductive SPM tip/PZT thin film/bottom metal capacitor, where the vertical SPM tip acts as the top electrode that can be precisely positioned and moved in a program-controlled way, dc and ac voltages [ $V_{dc}$  and  $V_{ac} \cos(\omega t)$ ] are applied simultaneously between the tip and the bottom metal,

$$V_{tip} = V_{dc} + V_{ac} \cos(\omega t), \quad (19)$$

set up electric field (E) and induce piezo electric oscillation ( $\delta$ ) on PZT surface,

$$\delta = \delta_0 + \delta_1 \cos(\omega t + \phi_1) + \delta_2 \cos(2\omega t + \phi_2) + \dots \quad (20)$$

which is actually detected by SPM as a voltage signal (V),

$$V = V_0 + V_1 \cos(\omega t + \phi_1) + V_2 \cos(2\omega t + \phi_2) + \dots \quad (21)$$

Where the subscript  $i$  ( $=0,1,2,\dots$ ) stands for the  $i$ th harmonic component,  $\phi_i - \phi_i$  is the  $i$ th harmonic phase shift of the SPM detecting system, phase  $\phi_1=0$  and  $\pi$  when the polarization vector  $P$  is up and down in the local domain. Of the harmonic components of various orders, the dc or static components reflect the surface topography if  $V_{dc}=0$ ; the 1st harmonic component reflects local piezo electric properties,

$$\delta_1 = d_{33} V_{ac}, \quad (22)$$

where  $d_{33}$  is the local piezoelectric constant,  $V_1$ ,  $\delta_1$ , and  $d_{33}$  are proportional to the magnitude of polarization ( $P$ ) and their sign reflects the  $P$  direction. With  $V_{dc} = 0$ ,  $P$  is the

spontaneous polarization  $P_s$ . For each tip position, if  $V_{dc}$  is swept and  $d_{33}$  is measured,  $d_{33}$  can be plotted against  $V_{dc}$  as a local piezoelectric curve [68].

The local piezoelectric curve is not the same as the better-known polarization ( $P$  versus  $E$ ) curve in macroscale. Usually,  $E$  is considered to be more pertinent than  $V_{dc}$  for properties characterization. However,  $d_{33}$  has not been plotted against  $E$ , mainly due to the difficulties in calculating  $E$  from  $V_{dc}$ . The actual interaction between the SPM tip and PZT thin film has been modeled using the layer capacitor model, the method of image charges, and the finite element analysis (FEA) [Harnagea, 2007]. In these cases, the approximate azimuthal symmetry reduces the problem into two dimensions [Lanyi et al, 1997].

PRI was conducted on electrospun PZT microfibers using a Dimension™ 3100 SPM by Digital Instruments under the conditions:  $V_{dc} = 0V$ ,  $V_{ac} = 10V$ ,  $\omega = 140\pi KHz$ . Figure 26 show typical SPM topography and PRI micrographs of a single fiber about  $5\mu m$  in diameter and an area within that fiber. Despite of the continuous surface topography [Fig. 26 (a)], PRI micrographs reveal numerous spontaneous polarization domains of size from 100 to 1000 nm [Figs. 26(b), 26(c)]. Their bright, dark, and grey colors correspond to up, down, and horizontal polarization directions, respectively.

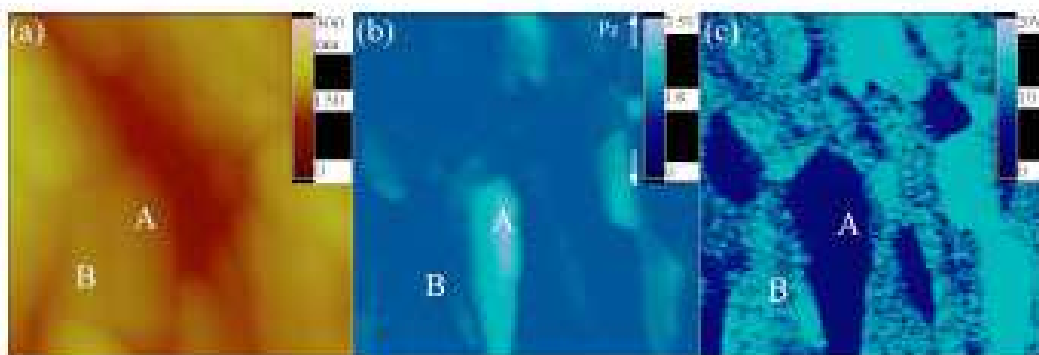


Fig. 26. (Color) (a) SPM topography, (b) PRI amplitude, and (c) PRI phase images of a single PZT microfiber (the area size is  $5 \times 5 \mu m^2$ ).

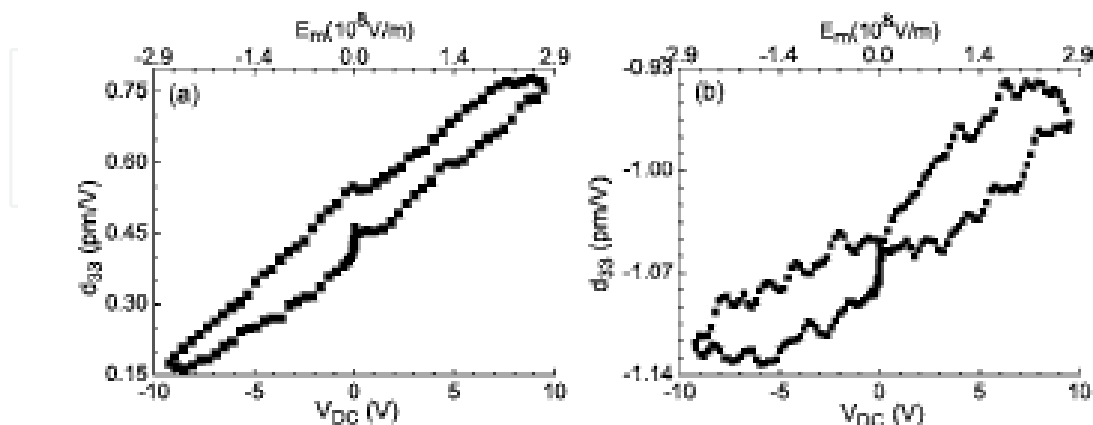


Fig. 27. Local  $d_{33}$  vs.  $V_{dc}$  curves of domains (a) A and (b) B in Fig. 26

During our local measurement, the SPM tip was positioned on two neighboring domains with opposite polarization direction (Fig. 26) and  $V_{dc}$  was swept in a cyclic way of  $0V \rightarrow 10V$

$V \rightarrow -10 \text{ V} \rightarrow 0 \text{ V}$  with a step of  $\pm 0.1 \text{ V}$ . Figure 27 presents local piezoelectric curves as  $d_{33}$  against  $V_{dc}$  and  $E_{max}$  using Eq. (17) with  $r=35 \text{ nm}$ . Note that  $d_{33}$  keeps its sign in both curves, implying that the polarization was not switched in two domains. Although  $E_{max}$  is as high as  $2.9 \times 10^8 \text{ V/m}$ ,  $E$  diminishes rapidly toward the bottom metal.

#### 4. References

- Abeles B., Sheng P., Coutts M. D., and Arie Y. (1975). Structural and electrical properties of granular metal- films. *Adv. Phys*, vol. 24, no. 3, 407-16.
- Amalric-Popescu D and Bozon-Verduraz F (2001), *Catal. Today*, 70, 139-154
- Bahl O. P., Shen Z, Lavin J. G., and. Ross R. A (1998). Manufacture of carbon fibers, *Carbon Fibers, 3rd ed*, Donnet J.-B., Ed, Marcel Dekker, New York, 1-84
- Baker D. F. and Bragg R. H. (1983). One-dimensionality in glassy carbon, *Phys. Rev. B*, vol. 28, no. 4, 2219- 2221
- Barsan N. and Weimar U. (2003), *Journal of Physics: Condensed Matter*, 15, R813-R839
- Bardeen J., Blatt F. J. and. Hall L. H (1954) *Photoconductivity Conference, Atlantic City*, Breckenridge R. G., Russell B. R and Hahn E. E., Ed, John Wiley, New York,
- Batzill M and Diebold U (2005) *Prog. Surf. Sci* 1956. 79, 47-154
- Bayot V., Piraux L., Michenaud J.-P., and Issi J.-P. (1989), *Phys. Rev. B* 40, 3514-3519
- Bayot V, Piraux L., Michenaud J.-P., and Issi J.-P. (1989), Weak localization in pregraphitic carbon fibers, *Phys. Rev. B*, vol. 40, no. 6, 3514-3523
- Bayot V., Piraux L., Michenaud J. P., Issi J. P., Lelaurain M., and Moore A. (1990), Two-dimensional weak localization in partially graphitic carbons, *Phys. Rev. B*, vol. 41, no. 17, 11 770-11 778
- Bergmann G. (1984), Weak localization in thin films a time of flight experiment with conduction electrons, *Phys. Rep* 107, 1, 1-58
- Birk H., Glatz-Reichenbach J., Jie L, Schreck E., and Dransfeld K., J. (1991), *Vac. Sci. Technol.* B 9, 1162-1166.
- Bright A. (1979) Negative magnetoresistance of pregraphitic carbons *Phys. Rev. B*, vol. 20, no. 12, 5142-5149
- Bright A. A and Singer L. S. (1979) Electronic and structural characteristics of carbon fibers from mesophase pitch. *Carbon*, vol. 17, 59-69.
- Bright A. A. and Singer, L. S. (1979), *Carbon* 17, 59-64
- Brinker C., Hurd A., Schunk P., Frye G. and Ashley C. (1992), *J. Non-Cryst. Solids* 147/148, 424-429
- Brunauer S., Emmett P. H. and Teller E. (1938) *J. Am. Chem. Soc.* 60, 309-319
- Burstein E. (1954) *Physl Rev*, 93,632-637
- Candeloro P., (2005), *Microelectronic Engineering*, 78, 178-185.
- Capone S., Siciliano P., Quaranta F., Rella R., Epifani M. and Vasanelli L. (2001), *Sensors Actuators B* 77, 503-511
- Comini E., (2002) *Applied Physics Letters*, 81, 1869-1875.
- Chopra K. L., Major S., and Panda D. K. (1983), Transparent Conductors- A status Review, *Thin Solid Films*, 102, 1-46.
- Chuah D. S. and Fun H. (1986), *Mater. Lett.* 4, 274-277
- Davazoglou D. (1997), *Thin Solid Films* 302, 204-213
- Deng Y., Dixon J. B. and White G. N. (2006), *Colloid Polym. Sci.*, 284, 347-356
- Dharmaraj N., Kim C. H., Kim K. W., Kim H. Y., Suh E. K. (2006), *Spectrochimica Acta Part A* 64, 136-140

- Doshi J. and Reneker D. H. (1995) Electrospinning process and application of electrospun fibers, *J. Electr.*, 35, 151–156
- Duan X., Huang Y., Wang J., and Lieber C. M. (2001), Indium phosphid nanowires as building blocks for nanoscale electronic and optoelectronic devices, *Nature*, 409, 66–69
- Duan X., Huang Y., Wangand J., and Lieber C. M. (2001)., *Nature (London)* 409, 66-72
- Endo M., Kim Y. A., Takeda T., Hong S. H., Matusita T., Hayashi T., and Dresselhaus M. S.(2001), Structural characterization of carbon nanofibers obtained by hydrocarbon pyrolysis, *Carbon*,. 39, 2003–2010.
- Endo M., Hishiyama Y., and Koyama T. (1982), Magnetoresistance effect in graphitizing carbon fibers prepared by benzene decomposition, *J. Phys. D, Appl. Phys.*, 15, 353–363.
- Faißt A. and Löhneysen H. V. (2002), Electrical resistance and magnetoresistance of pyrocarbon at Low temperatures in fields up to 14 tesla, *Carbon*, vol. 40, 321–327.
- Fiaz A., Ali S., Parvez M., Munir A., Khan K. M., Shah T. A. and Mazhar M. (2002), *Heteroatom Chem.* 13 638–649
- Formhals A. (1934), *Process and Apparatus for Preparing Artificial Threads*, U.S. Pat. 1 975 504
- Fuji M., Matsui M., Motojima S., and Hishikawa Y. (2002), Magnetoresistance in carbon micro-coils obtained by chemical vapor deposition, *Thin Solid Films*, 409, 78–81.
- Giraldi T. R., Escote M. T., Maciel A. P, Longo E., Leite E. R, Varela J. A. (2006), *Thin Solid Films*, 515, 2678-2685.
- Gopel W. and Schierbaum K.D. (1995), *Sensors and Actuators B*, 26, 1-8
- Harnagea C. (2001), *Local piezoelectric response and domain structures in ferroelectric thin films investigated by voltage-modulated force microscopy*, Ph.D. thesis; <http://sundoc.bibliothek.uni-halle.de/diss-online/01/01H318>, June 23, 2007.
- Hishiyama Y. (1976), Negative magnetoresistance in soft carbons and graphite, *Carbon*,. 8, 259–269
- Hori M., Hattori S., Yoneda T. and Morita S. (1986), *J. Vac. Sci. Technol. B*, 4, 500–504
- Hu J., Odom T. W., and Lieber C. M. (1999), Chemistry and physics in one dimension: Synthesis and properties of nanowires and nanotubes, *Acc. Chem. Res.*, 32, 435–445
- Hu J., Odom T. W., and Lieber C. M, (1999), *Acc. Chem. Res.* 32, 435-441
- Inagaki M and Radovic L. R. (2002)., *Carbon* 40, 2279-2287
- Ishioka M., Okada T., and Matsubara K. (1993), Electrical resistivity, magnetoresistance, and morphology of vapor-grown carbon fibers prepared in a mixture of benzene and Linz-Donawitz converter gas by floating catalyst method, *J. Mater. Res.*, 8, 8, 1866–1874.
- Jackson J. D. (1999), *Classical Electrodynamics*, 3rd ed., Wiley, New York
- JCPDS Card No. 41-1445, 27-1402, 41-1445
- Japanese National Institute of Advanced Industrial Science and Technology. (2006), *Spectral Database for Organic Compounds* available at [http://www.aist.go.jp/RIODB/SDBS/cgi-bin/cre\\_index.cgi](http://www.aist.go.jp/RIODB/SDBS/cgi-bin/cre_index.cgi)
- Jarzebski Z. M. and Marton J. P. (1976), *Journal of Electrochemical Society*, 123 199C-205C, 123 (1976): 299C-310C, 123 (1976): 333C-346C.
- Jensen J. O. (2004), *Spectrochim. Acta A*, 60, 2561-2570
- Jin Z., Zhou H-J., Jin Z-L., Savinell R. F. and Liu C-C. (1998), *Sensors Actuators B*, 52, 188–194
- Klein C. A. (1964), STB model and transport properties of pyrolytic graphites, *J. Appl. Phys.*, 35, 10, 2947–2957.
- Koike Y. and Fukase T. (1987), Anomalous electrical conduction in carbon fibers at low temperatures, *Solid-State Commun.*, 62, 6, 499–502
- Kolmakov A., Zhang Y., Cheng G., and Moskovits M. (2003), *Adv. Mater.* 15 (12), 997-1003
- Korotchenkov G., Brynzari V. and Dmitriev S. (1999), *Sensors Actuators B* 54, 197–201

- Kolmakov A. and Moskovits M. (2004), *Annu. Rev. Mater. Res.*, 34, 151-170
- Kwag G. (2002), *Macromolecules* 35, 4875-4879
- Langer L., Bayot V., Grivei E., Issi J.-P., Heremans J. P., Olk C. H., Stockman L., Van Haesendonck C., and Bruynseraede Y. (1996), Quantum transport in a multiwalled carbon nanotube, *Phys. Rev. Lett.*, 76, 3, 479-482
- Lanyi S., Torok J., and Rehurek P. (1996), *J. Vac. Sci. Technol. B*, 14, 892-897
- Law M., Goldberger J. and Yang P. (2004), *Annu. Rev. Mater. Res.*, 34, 83-88.
- Lee P. A. and Ramakrishnan T. V. (1985), Disordered electronic system, *Rev. Modern Phys.*, 57, 2, 287-337.
- Lehmann V., Gosele U. (1991), *Appl. Phys. Lett.*, 58, 856-860
- Liu Z., Zhang D., Han S., Li C., Tang T., Jin W., Liu X., Lei B. and Zhou C. (2003), *Adv. Mater.* 15, 1754-1762
- Li D., Wang Y. and Xia Y. (2003), *Nano Lett.*, 3, 1167-1173
- Mandayo G. G., Castano E., Gracia F. J., Cirera A., Cornet A. and Morante J. R. (2003), *Sensors Actuators B* 95, 90-96
- Mathur S., Barth S., Shen H., Pyun J. and Werner U. (2005), *Small*, 1, 7713-7717.
- Mishra S., Ghanshyam C., Ram N., Singh S., Bajpai R. P. and Bedi R. K. (2002), *Bull. Mater. Sci.*, 25, 231-245
- Moss T. S. (1954), *Proceedings of Physics Society London B*, 67, 775-791.
- Mott N. F. and Davis E. A. (1979), *Electronic Processes in Non-Crystalline Materials*. Oxford, Clarendon Press, U.K.
- Moulder J.F. et al. (1992), *Handbook of X-Ray Photoelectron Spectroscopy*, Jill Chastain, (by Perkin-Elmer Corporation, Physical Electronics Division, Minnesota, USA,).
- Mrozowski S. (1979), Specific-heat anomalies and spin-spin interactions in carbons—Review, *J. Low Temp Phys.*, 35, 3/4, 231-297.
- Mrozowski S. and Chaberski A. (1956), Hall effect and magnetoresistivity in carbons and polycrystalline graphites, *Phys. Rev.*, 104, 74, 74-83
- Naoyoshi T. (1975), Japanese Patent No. S50-30480
- NIST Chemistry Webbook, NIST Standard Reference Database Number 69, (2005), Release available at <http://webbook.nist.gov/chemistry> Nov 5, 2006
- Pouchert C. J. (1997), *The Aldrich Library of FT-IR Spectra 2<sup>nd</sup> edn*, vol 1-4 (Wisconsin, USA: Sigma-Aldrich Co.)
- Putley E. H. (1960), *The Hall Effect and Related Phenomena*, 66-97, Butterworth, London, U.K.
- Ratna D., Divekar S., Samui A. B., Chakraborty B. C. and Banthia A. K. (2006), *Polymer* 47, 4068-4074
- Rebbouillat S., Peng J. C. M., Donnet J.-B., and Ryu S.-K. (1998), *Carbon Fibers, 3rd ed*, Donnet J.-B., Wang T. K., and Peng J. C. M., Eds, 463-542, Marcel Dekker, , New York
- Renker D. H. and Chun I. (1996), Nanometer diameter fibers of polymer, produced by electrospinning, *Nanotechnology*, 7, 216-223
- Rosenbaum R. (1985), Superconducting fluctuations and magnetoconductance measurements of thin films in parallel magnetic fields, *Phys. Rev. B*, 32, 4, 2190-2199
- Ryzhikov I. A., Pukhov A. A., Il'in A. S., Glukhova N. P., Afanasiev K. N. and Ryzhikov A. S. (2003) *Microelectron. Eng.*, 69, 270-273
- Sacher R. E., Davidsohn W. and Miller F. A. (1970), *Spectrochim. Acta* 26, 1011-1022
- Santhi E., Dutta V., Banjeree A. and Chopra K. L. (1980), *J. Appl. Phys.*, 51, 6243-6249
- Santiago-Aviles J.J. and Wang Y. (2003), *Carbon*, 41, 2665-2670.
- Scott J.F. (1970), *J. Chem Phys*, 53, 852-855
- Seal S. and Shukla S. (2002), Nanocrystalline SnO gas sensors in view of surface reactions and modifications, *Journal of Metals*, 54, 9, 35-60

- Shaw T. M., Trolier-McKinstry S., and McIntyre P. C. (2000), *Annu. Rev. Mater. Sci.*, 30, 263-284
- Shanthi S., Subramanian C., Ramasamy P. (1999), *Crystal Research and Technology*, 34, 8, 1037-1046
- Sinclair W., Peters F., Stillinger D. and Koonce S. (1965), *J. Electrochem. Soc.*, 112, 1096-1100
- Silverstein R. M. and Webster F. X. (1998), *Spectrometric Identification of Organic Compound 6th edn* Wiley, New York
- Spain I. L., Volin K. J., Goldberg H. A., and Kalnin I. (1983), Electronic properties of pan-based carbon fibers, *J. Phys. Chem. Solids*, 44, 8, 839-849.
- Tang A. (1997), *Sensors and Actuators B*, 43, 161-172.
- Terrier C., Chatelon J. P. and Roger J. A. (1997), *Thin Solid Films*, 295, 95-100
- Trolier-McKinstry S. and Muralt P. (2004), *J. Electroceram.*, 12, 7-16
- Wang Y., Serrano S., and Santiago-Aviles J. J. (2002), Conductivity measurement of electrospun PAN-based carbon nanofiber, *J. Mater. Sci. Lett.*, 21, 1055-1057.
- Wang Y., Serrano S. and Santiago-Avilés J. J. (2002), *Materials Research Society, Symposia Proceedings Vol. 702* Materials Research Society, Pittsburgh, 359-362.
- Wang Y. and Santiago-Aviles J. J. (2002), *Mater. Res. Soc. Symp. Proc. 702*, 235-340
- [a], Wang Y., Santiago-Aviles J. J., Furlan R., and Ramos I. (2003), Pyrolysis temperature and time dependence of electrical conductivity evolution for electrostatically generated carbon nanofibers, *IEEE Trans. Nanotechnol.*, 2, 39-43
- Wang Y. and Santiago-Avilés J. J. (2003), Large negative magnetoresistance and two-dimensional weak localization in carbon nanofiber fabricated using electrospinning, *J. Appl. Phys.*, 94, 3, 1721-1727
- [b], Wang Y., Serrano S., and Santiago-Aviles J. J. (2003), Raman characterization of carbon nanofibers prepared using electrospinning, *Synthetic Metals*, 138, 423-427
- Wang Y. and Santiago-Avilés J. J. (2004), *Nanotechnology*, 15, 32-37
- [a], Wang Y., Furlan R., Ramos I. and Santiago-Aviles J. J. (2004), *Appl. Phys. A*, 78, 1043-1047
- [b], Wang Y., Aponte M., Leon N., Ramos I., Furlan R., Evoy S. and Santiago-Avilés J. J. (2004), *Semicond. Sci. Technol.*, 19, 1057-1061
- [c], Wang Y., Aponte M., Leon N., Ramos I. (2004), Synthesis and characterization of tin oxide microfibers electrospun from a simple precursor solution, *Semicond. Sci. Tech.*, 19, 1057-1062.
- [a], Wang Y., Aponte M., Leon N., Ramos I., Furlan R., Pinto N., Evoy S. and Santiago-Avilés J. J. (2005), *J. Am. Ceram. Soc.*, 88, 2059-2063
- [b], Wang Y., Aponte M., Leon N., Ramos I. (2005), *J. Am. Ceram. Soc.* 88, 8, 2059-2064.
- Wang Y., Ramos I., and Santiago-Avilés J. (2007), Synthesis of ultra-fine porous tin oxide fibers and its process characterization, *Nanotech.*, 18, 7, 295601-295607
- Xu C., Xu G., Liu Y., Zhao X. and Wang G. (2002), *Scr. Mater.*, 46, 789-793
- Ye J. D., Gu S. L., Zhu S. M., Liu S. M. Zhang., Y. D, Zhang R., Shi Y. (2005), *Appl. Phys. Lett.*, 86, 19, 2111-2117
- Ying T. H., Sarmadi A. M., Hop C. E. C. A. and Denes F. (1995), *J. Appl. Polym. Sci.*, 55, 1537-1551
- Yoshikawa S., Selvaraj U., Moses P., Withams J., Meyer R, and Shrout T. (1995), *J. Intell. Mater. Syst. Struct.*, 6, 152-158
- Watson J. (1984), *Sensors and Actuators*, 5, 29-35.
- Williams D. (1987), *Solid State Gas Sensors*, 71-87, P Moseley and B Tofield, Ed, Hilger Bristol U.K.



## **Nanofibers**

Edited by Ashok Kumar

ISBN 978-953-7619-86-2

Hard cover, 438 pages

**Publisher** InTech

**Published online** 01, February, 2010

**Published in print edition** February, 2010

“There's Plenty of Room at the Bottom” this was the title of the lecture Prof. Richard Feynman delivered at California Institute of Technology on December 29, 1959 at the American Physical Society meeting. He considered the possibility to manipulate matter on an atomic scale. Indeed, the design and controllable synthesis of nanomaterials have attracted much attention because of their distinctive geometries and novel physical and chemical properties. For the last two decades nano-scaled materials in the form of nanofibers, nanoparticles, nanotubes, nanoclays, nanorods, nanodisks, nanoribbons, nanowiskers etc. have been investigated with increased interest due to their enormous advantages, such as large surface area and active surface sites. Among all nanostructures, nanofibers have attracted tremendous interest in nanotechnology and biomedical engineering owing to the ease of controllable production processes, low pore size and superior mechanical properties for a range of applications in diverse areas such as catalysis, sensors, medicine, pharmacy, drug delivery, tissue engineering, filtration, textile, adhesive, aerospace, capacitors, transistors, battery separators, energy storage, fuel cells, information technology, photonic structures and flat panel displays, just to mention a few. Nanofibers are continuous filaments of generally less than about 1000 nm diameters. Nanofibers of a variety of cellulose and non-cellulose based materials can be produced by a variety of techniques such as phase separation, self assembly, drawing, melt fibrillation, template synthesis, electrospinning, and solution spinning. They reduce the handling problems mostly associated with the nanoparticles. Nanoparticles can agglomerate and form clusters, whereas nanofibers form a mesh that stays intact even after regeneration. The present book is a result of contributions of experts from international scientific community working in different areas and types of nanofibers. The book thoroughly covers latest topics on different varieties of nanofibers. It provides an up-to-date insightful coverage to the synthesis, characterization, functional properties and potential device applications of nanofibers in specialized areas. We hope that this book will prove to be timely and thought provoking and will serve as a valuable reference for researchers working in different areas of nanofibers. Special thanks goes to the authors for their valuable contributions.

### **How to reference**

In order to correctly reference this scholarly work, feel free to copy and paste the following:

Yu Wang, Idalia Ramos and Jorge J. Santiago-Aviles (2010). Diversity of Nanofibers from Electrospinning: from Graphitic Carbons to Ternary Oxides., Nanofibers, Ashok Kumar (Ed.), ISBN: 978-953-7619-86-2, InTech, Available from: <http://www.intechopen.com/books/nanofibers/diversity-of-nanofibers-from-electrospinning-from-graphitic-carbons-to-ternary-oxides->

# INTECH

open science | open minds

## **InTech Europe**

University Campus STeP Ri  
Slavka Krautzeka 83/A  
51000 Rijeka, Croatia  
Phone: +385 (51) 770 447  
Fax: +385 (51) 686 166  
[www.intechopen.com](http://www.intechopen.com)

## **InTech China**

Unit 405, Office Block, Hotel Equatorial Shanghai  
No.65, Yan An Road (West), Shanghai, 200040, China  
中国上海市延安西路65号上海国际贵都大饭店办公楼405单元  
Phone: +86-21-62489820  
Fax: +86-21-62489821

IntechOpen

IntechOpen

© 2010 The Author(s). Licensee IntechOpen. This chapter is distributed under the terms of the [Creative Commons Attribution-NonCommercial-ShareAlike-3.0 License](#), which permits use, distribution and reproduction for non-commercial purposes, provided the original is properly cited and derivative works building on this content are distributed under the same license.

IntechOpen

IntechOpen